J. Fluid Mech. (2011), *vol.* 687, *pp.* 300–340.
doi:10.1017/jfm.2011.353

The decay of turbulence generated by a class of multiscale grids

P. C. Valente† and J. C. Vassilicos†

Department of Aeronautics, Imperial College London, London SW7 2AZ, UK

(Received 17 December 2010; revised 18 August 2011; accepted 21 August 2011;
first published online 12 October 2011)

A new experimental investigation of decaying turbulence generated by a low-blockage space-filling fractal square grid is presented. We find agreement with previous works by Seoud & Vassilicos (*Phys. Fluids*, vol. 19, 2007, 105108) and Mazellier & Vassilicos (*Phys. Fluids*, vol. 22, 2010, 075101) but also extend the length of the assessed decay region and consolidate the results by repeating the experiments with different probes of increased spatial resolution. It is confirmed that this moderately high Reynolds number Re_λ turbulence (up to $Re_\lambda \simeq 350$ here) does not follow the classical high Reynolds number scaling of the dissipation rate $\varepsilon \sim u'^3/L$ and does not obey the equivalent proportionality between the Taylor-based Reynolds number Re_λ and the ratio of integral scale L to the Taylor microscale λ. Instead we observe an approximate proportionality between L and λ during decay. This non-classical behaviour is investigated by studying how the energy spectra evolve during decay and examining how well they can be described by self-preserving single-length-scale forms. A detailed study of homogeneity and isotropy is also presented which reveals the presence of transverse energy transport and pressure transport in the part of the turbulence decay region where we take data (even though previous studies found mean flow and turbulence intensity profiles to be approximately homogeneous in much of the decay region). The exceptionally fast turbulence decay observed in the part of the decay region where we take data is consistent with the non-classical behaviour of the dissipation rate. Measurements with a regular square mesh grid as well as comparisons with active-grid experiments by Mydlarski & Warhaft (*J. Fluid Mech.*, vol. 320, 1996, pp. 331–368) and Kang, Chester & Meveneau (*J. Fluid Mech.*, vol. 480, 2003, pp. 129–160) are also presented to highlight the similarities and differences between these turbulent flows and the turbulence generated by our fractal square grid.

Key words: isotropic turbulence, turbulence theory

1. Introduction

At high enough Reynolds numbers, the local viscous dissipation rate ε of the local average turbulent kinetic energy K scales with K and a local correlation length scale L, i.e. $\varepsilon \sim K^{3/2}/L$. At least, this is what one reads in turbulence textbooks (see, for example, Batchelor 1953; Townsend 1956; Tennekes & Lumley 1972; Lumley 1992; Frisch 1995; Lesieur 1997; Mathieu & Scott 2000; Pope 2000; Sagaut & Cambon 2008). Tennekes & Lumley (1972) introduce this scaling in their very first chapter

† Email addresses for correspondence: p.valente09@imperial.ac.uk,
j.c.vassilicos@imperial.ac.uk

with the words 'it is one of the cornerstone assumptions of turbulence theory'. Townsend (1956) uses it explicitly in his treatment of free turbulent shear flows (see page 197 in Townsend 1956) which includes wakes, jets, shear layers, etc. Since Taylor introduced it in 1935 (Taylor 1935), this scaling has also customarily been used in theories of decaying homogeneous isotropic turbulence (see Batchelor 1953; Rotta 1972; Frisch 1995) and in analyses of wind-tunnel simulations of such turbulence (e.g. Batchelor & Townsend 1948; Comte-Bellot & Corrsin 1966) in the form

$$\varepsilon = C_\varepsilon \frac{u'^3}{L} \tag{1.1}$$

where u' is the root mean square (r.m.s.) velocity fluctuation, L is an integral length scale and C_ε is a constant independent of time, space and Reynolds number when the Reynolds number is large enough. However, as Taylor (1935) was careful to note, the constant C_ε does not need to be the same irrespective of the boundaries (initial conditions) where the turbulence is produced (see Burattini, Lavoie & Antonia 2005; Mazellier & Vassilicos 2008; Goto & Vassilicos 2009).

In high Reynolds number self-preserving free turbulent shear flows, the cornerstone scaling $\varepsilon \sim K^{3/2}/L$ determines the entire dependence of ε on the streamwise coordinate and ascertains its independence of Reynolds number (see Townsend 1956). This cornerstone scaling is also effectively used in turbulence models such as $K-\varepsilon$ (see Pope 2000) and in large-eddy simulations (see Lesieur 1997; Pope 2000). The assumption that ε is independent of Reynolds number when the Reynolds number is large enough is an inseparable part of the Richardson–Kolmogorov cascade (Tennekes & Lumley 1972; Frisch 1995). This is the celebrated nonlinear dissipation mechanism of the turbulence whereby, within a finite time $L/\sqrt{K}$ (the same time scale for all high enough Reynolds numbers), smaller and smaller 'eddies' are generated until eddies so small are formed which can very quickly lose their kinetic energy by linear viscous dissipation. The higher the Reynolds number, the smaller the size of these necessary dissipative eddies but the time scale $L/\sqrt{K}$ for energy to cascade to them from the large eddies remains the same. The dissipation rate ε is proportional to K divided by this time, and therefore $\varepsilon \sim K^{3/2}/L$.

In various high Reynolds number self-preserving free turbulent shear flows as in wind-tunnel grid-generated turbulence, K and L vary with streamwise downstream distance $x-x_0$ (where x_0 is an effective/virtual origin) as power laws. Specifically, $K \sim U_\infty^2((x-x_0)/L_B)^{-n}$ and $L \sim L_B((x-x_0)/L_B)^m$ where L_B is a length scale characterizing the inlet and U_∞ is the appropriate inlet velocity scale. In table 1 we recall the generally accepted values taken by the exponents n and m in plane wakes, axisymmetric wakes, self-propelled plane wakes, self-propelled axisymmetric wakes, mixing layers, plane jets, axisymmetric jets and wind-tunnel grid-generated turbulence (from Comte-Bellot & Corrsin 1966; Tennekes & Lumley 1972). Estimating a Taylor microscale λ from $\varepsilon \sim \nu K/\lambda^2$ where ν is the kinematic viscosity of the fluid, and then applying the cornerstone assumption $\varepsilon \sim K^{3/2}/L$ to all these flows yields the following two relations:

$$L/\lambda \sim Re_0^{1/2}\left(\frac{x-x_0}{L_B}\right)^{(m/2)-(n/4)} \tag{1.2}$$

and

$$\sqrt{K}\lambda/\nu \sim Re_0^{1/2}\left(\frac{x-x_0}{L_B}\right)^{(m/2)-(n/4)} \tag{1.3}$$

	K	L	L/λ
Plane wake	1	1/2	0
Axisymmetric wake	4/3	1/3	−1/6
Self-propelled plane wake	3/2	1/4	−1/4
Self-propelled axisymmetric wake	8/5	1/5	−3/10
Mixing layer	0	1	1/2
Plane jet	1	1	1/4
Axisymmetric jet	2	1	0
Regular grid turbulence	1.25	0.35	−0.14

TABLE 1. Power law exponents characteristic of the downstream evolutions of K, L and L/λ.

where $Re_0 \equiv U_\infty L_B/\nu$ is the inlet Reynolds number and $\sqrt{K}\lambda/\nu$ is a local Taylor microscale-based Reynolds number. The different values of $(m/2) - (n/4)$ are given in table 1. Remarkably, $\varepsilon \sim K^{3/2}/L$ implies that $L/\lambda \sim \sqrt{K}\lambda/\nu$ in all of these flows regardless of the values of n and m, meaning that $L/\lambda \sim \sqrt{K}\lambda/\nu$ collapses the Re_0 and the x dependencies in the same way for all of these flows. We stress that this collapse is the immediate consequence of $\varepsilon \sim K^{3/2}/L$. The relation $L/\lambda \sim \sqrt{K}\lambda/\nu$ simply reflects the Richardson–Kolmogorov cascade: the higher the Reynolds number, the smaller the size of the dissipative eddies, i.e. the greater the range of excited scales and the greater L/λ.

As noted by Lumley (1992), by 1992 there had not been too much detailed and comprehensive questioning of data to establish the validity of $\varepsilon \sim K^{3/2}/L$ but he wrote: 'I hardly think the matter is really much in question'. He cited the data compilations of Sreenivasan (1984) which suggested that C_ε does become constant at $Re_\lambda = u'\lambda/\nu$ larger than about 50 for wind-tunnel turbulence generated by various biplane square-mesh grids, but there seemed to be little else at the time. Since then, direct numerical simulations (DNSs) of high Reynolds number statistically stationary homogeneous isotropic turbulence have significantly strengthened support for the constancy of C_ε at Re_λ greater than about 150 (see the compilation of data in Burattini *et al.* 2005; see also Sreenivasan 1998). Other turbulent flows have also been tried in the past fifteen years or so such as various turbulent wakes and jets and wind-tunnel turbulence generated by active grids (see Burattini *et al.* 2005; Mazellier & Vassilicos 2008) with some, perhaps less clear, support of the constancy of C_ε at large enough Re_λ (perhaps larger than about 200 if L is defined appropriately, see Burattini *et al.* 2005) and also some clear indications that the high Reynolds number constant value of C_ε is not universal, as indeed cautioned by Taylor (1935).

A decade ago, Queiros-Conde & Vassilicos (2001) took the opposite approach and asked whether it might be possible to break $\varepsilon \sim K^{3/2}/L$ in some fundamental way in some flows, and so they proposed generating turbulence with fractal/multiscale objects/stirrers/inlet conditions. Some years later, Hurst & Vassilicos (2007) published an exploratory study of wind-tunnel grid-generated turbulence where they tried 21 different planar grids from 3 different families of passive fractal/multiscale grids: fractal cross grids, fractal I grids and fractal square grids (FSGs). They ascertained that the fractal dimension D_f of these grids needs to take the maximal value $D_f = 2$ for the least downstream turbulence inhomogeneity. They also identified some important grid-defining parameters (such as the thickness ratio t_r, see figure 1 and table 3)

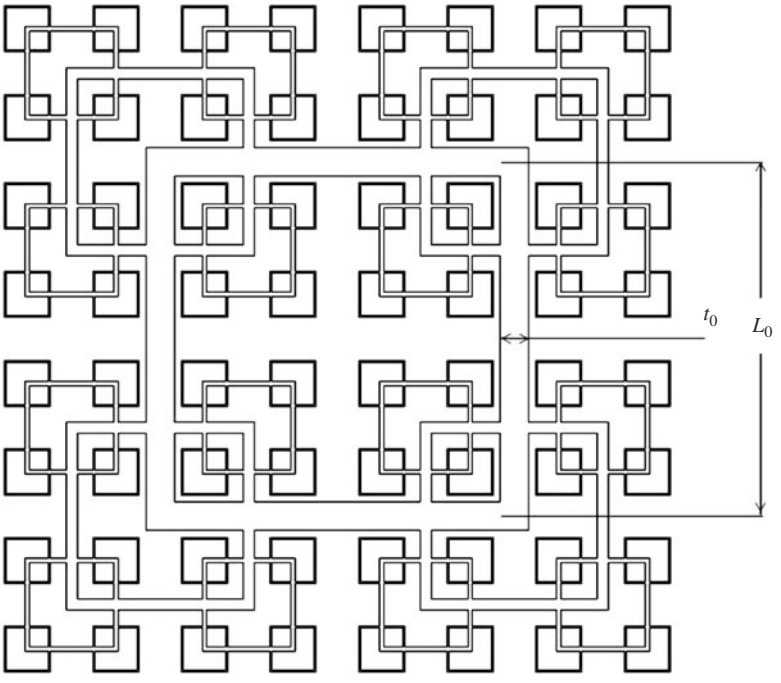

FIGURE 1. Low-blockage space-filling FSG. The grid is space filling because the fractal dimension of its delimiting line takes the maximum value of 2 over the range of scales on the grid. In the limit of infinite number of fractal iterations the blockage ratio will tend to unity, without taking bar thickness into account. However with only four iterations and the bar thickness in the figure the grid's blockage ratio is only 25 %.

and some of their effects on the flow, in particular on the Reynolds number Re_λ which they showed can reach high values with some of these grids in small and conventional sized wind tunnels, comparable to the values of Re_λ achieved with active grids in similar wind tunnels and wind speeds. Their most interesting, and in fact intriguing, results were for their space-filling ($D_f = 2$) low-blockage (25 %) FSGs (see figure 1). FSGs have therefore been the multiscale grids of choice in most subsequent works on multiscale/fractal-generated turbulence (Seoud & Vassilicos 2007; Nagata *et al.* 2008*a*,*b*; Stresing *et al.* 2010; Mazellier & Vassilicos 2010; Suzuki *et al.* 2010; Laizet & Vassilicos 2011). For the case of space-filling low-blockage FSGs, Hurst & Vassilicos (2007) found a protracted region between the grid and a distance x_{peak} downstream of the grid where the turbulence progressively builds up; and a decay region at $x > x_{peak}$ where the turbulence continuously decays downstream. They reported a very fast turbulence decay which they fitted with an exponential and also reported very slow downstream growths of the longitudinal and lateral integral length scales and of the Taylor microscale. (Very recently, Krogstad & Davidson 2011 studied the decay behind multiscale cross grids and found conventional decay rates. Note that for multiscale cross grids our prior publications did not claim fast, unconventional, decay rates (Hurst & Vassilicos 2007). This may serve as further justification for focusing attention on FSGs in the present paper. Even so, multiscale cross grids have been used successfully in some recent studies for enhancing the Reynolds number, see Geipel, Henry Goh & Lindstedt 2010 and Kinzel *et al.* 2011.)

Seoud & Vassilicos (2007) concentrated their attention on the decay region of turbulence generated by space-filling low-blockage FSGs and confirmed the results of Hurst & Vassilicos (2007). In particular, they showed that L/λ remains approximately constant whilst Re_λ decays with downstream distance x and they noted that this behaviour implies a fundamental break from (1.1) where C_ε is constant. They also found that one-dimensional longitudinal energy spectra at different downstream centreline locations x can be made to collapse with u' and a single length scale, as opposed to the two length scales (L and Kolmogorov microscale) required by Richardson–Kolmogorov phenomenology. Finally, they also carried out homogeneity assessments in terms of various profiles (mean flow, turbulence intensity, turbulence production rate) as well as some isotropy assessments.

Mazellier & Vassilicos (2010) also worked on wind-tunnel turbulence generated by space-filling low-blockage FSGs. They introduced the wake-interaction length scale x_* which is defined in terms of the largest length and thickness on the grid and they showed from their data that $x_{peak} \approx 0.5x_*$. They documented how very inhomogeneous and non-Gaussian the turbulent velocity statistics are in the production region near the grid and how homogeneous and Gaussian they appear by comparison beyond $0.5x_*$. They confirmed the findings of Hurst & Vassilicos (2007) and Seoud & Vassilicos (2007) and added the observation that both Re_λ and L/λ are increasing functions of the inlet velocity U_∞. Thus, the value of L/λ seems to be set by the inlet Reynolds number, in this case defined as $Re_0 = U_\infty x_*/\nu$ for example.

Finally, Mazellier & Vassilicos (2010) brought the two different single-scale turbulence decay behaviours of George (1992) and George & Wang (2009) into a single framework which they used to analyse the turbulence decay in the downstream region beyond $x_{peak} \approx 0.5x_*$. This allowed them to introduce and confirm against their data the notions that, in the decay region, the fast turbulence decay observed by Hurst & Vassilicos (2007) and Seoud & Vassilicos (2007) may not be exponential but a fast decaying power law and that L and λ are in fact increasing functions of x which keep L/λ approximately constant.

The results of Hurst & Vassilicos (2007), Seoud & Vassilicos (2007) and Mazellier & Vassilicos (2010) suggest that, in the decay region downstream of space-filling low-blockage FSGs, high Reynolds number turbulence is such that

$$L/\lambda \sim Re_0^\alpha A\left(\frac{x-x_0}{x_*}\right) \tag{1.4}$$

and

$$Re_\lambda \sim Re_0^\beta B\left(\frac{x-x_0}{x_*}\right) \tag{1.5}$$

where A is a slow-varying dimensionless function of $(x-x_0)/x_*$ (in fact, effectively constant), B is a fast-decreasing dimensionless function of $(x-x_0)/x_*$ (perhaps even as fast as exponential) and α and β are positive real numbers.

Assuming that the dissipation-scale turbulence structure is approximately isotropic, we now use the relation $\varepsilon = 15\nu u'^2/\lambda^2$ which Taylor (1935) obtained for isotropic turbulence. With (1.1) this relation implies

$$\frac{L}{\lambda} = \frac{C_\varepsilon}{15} Re_\lambda \tag{1.6}$$

and, clearly, C_ε cannot be constant (independent of Re_0 and x) with Re_0 and x dependencies of L/λ and Re_λ such as those observed in wind-tunnel turbulence

generated by space-filling low-blockage FSGs. Instead,

$$C_\varepsilon = 15Re_0^{\alpha-\beta}A\left(\frac{x-x_0}{x_*}\right)\Big/B\left(\frac{x-x_0}{x_*}\right) \tag{1.7}$$

which means that C_ε should be increasing fast in the downstream direction but which also means that a plot of C_ε versus Re_λ can be quite different depending on whether Re_λ is varied by varying Re_0 whilst staying at the same position x or by moving along x whilst keeping Re_0 constant. This is a point which we discuss and attempt to bring out clearly in the present paper.

Relations (1.4) and (1.5) and their consequent decoupling of L/λ and Re_λ were observed at moderate to high values of Re_λ where Seoud & Vassilicos (2007) and Mazellier & Vassilicos (2010) also observed a well-defined broad power-law energy spectrum. Indeed Re_λ needs to be large enough for the study of fully developed turbulence. Active grids were introduced by Makita (1991) to improve on the Reynolds number values achieved by regular grids (RGs) in conventional wind tunnels. FSGs achieve comparably high values of Re_λ but also a far wider range of Re_λ values along the streamwise direction. This makes it much easier to study Re_λ dependencies, a point which we make and discuss in some detail in the present paper.

In this paper we report an experimental assessment of turbulent flows generated by a low-blockage space-filling FSG (see figure 1) and a regular square-mesh grid. The main focus of this paper is to complement former research on fractal-generated turbulence by extending the assessed decay region and using the new data to re-address the previously reported dramatic departure from $C_\varepsilon = constant$ and $A((x-x_0)/x_*) = B((x-x_0)/x_*)$ and the abnormally high decay exponents (Hurst & Vassilicos 2007; Seoud & Vassilicos 2007; Mazellier & Vassilicos 2010). We provide estimates of these exponents, and also show that $\alpha \approx \beta$ and that our fractal-generated turbulence behaves in a way which is very close to self-preserving single-length scale turbulence (Mazellier & Vassilicos 2010), particularly if the turbulence anisotropy is taken into account when calculating three-dimensional energy spectra. We also show that, even though previous studies by Seoud & Vassilicos (2007) and Mazellier & Vassilicos (2010) found that the mean flow and turbulence profiles are approximately homogeneous in much of the decay region, there nevertheless remains significant transverse turbulent transport of turbulent kinetic energy and turbulent transport of pressure. The decaying turbulence is therefore not homogeneous and isotropic in terms of third-order one-point statistics even though it more closely is in terms of lower-order one-point statistics. Whenever possible a comparison between fractal-generated and non-fractal-generated turbulence is made emphasizing the similarities and differences.

In the following section we describe the experimental apparatus as well as the anemometry systems, probes and the details of the data acquisition. The experimental results are presented in § 3 and are organized into four subsections. In § 3.1 it is suggested that the wake-interaction length scale introduced by Mazellier & Vassilicos (2010) to characterize the extent of the production region in the lee of the fractal grid is also meaningful for regular static grids. In § 3.2 the homogeneity and isotropy of the fractal-generated flow is investigated following the methodology used by Corrsin (1963) and Comte-Bellot & Corrsin (1966) for regular static grids. In §§ 3.3 and 3.4 the normalized energy dissipation rate and the decay law are re-assessed using the new data. In § 3.5 we investigate the possibility of a self-similar, single-length-scale behaviour by collapsing the one-dimensional energy spectra and the second-order structure functions using large-scale variables; also the three-dimensional energy

spectrum function is calculated to provide isotropy corrections on the collapse. In § 4 we end this paper by highlighting the main conclusions drawn from the present measurements and discuss some of the questions raised.

2. The experimental setup

2.1. *Experimental hardware*

The experiments are performed in the $T = 0.46$ m wind tunnel described in some detail in Mazellier & Vassilicos (2010) and sketched in figure 5 (T is the lateral width of the tunnel's square test section). The inlet velocity U_∞ is imposed and stabilized with a PID feedback controller using the static pressure difference across the 8:1 contraction and the temperature near the inlet of the test section which are measured using a Furness Controls micromanometer FCO510.

All data are taken with one- and two-component hot-wire anemometers operating in constant-temperature mode (CTA). The hot wires are driven by a DANTEC StreamLine CTA system with an in-built signal conditioner. We use both square- and sine-wave testing to measure the cut-off frequency at the verge of attenuation ($f_{cut\text{-}off}^{0\ \mathrm{dB}}$) and at the standard '$-3$ dB' attenuation level ($f_{cut\text{-}off}^{-3\ \mathrm{dB}}$). In table 2 we present the results from the electronic testing of our anemometry system. Further information concerning electronic testing of thermal anemometers and a discussion of the consistency between the square and sine-wave tests can be found in Freymuth (1977).

For the single-component measurements three different single wires (SWs) are used with a sensing length (l_w) of 1 mm, 0.45 mm and 0.2 mm, respectively. For the two-component measurements, two cross wires (XWs) with sensing lengths of $l_w = 0.5$ and 1 mm, respectively, are used, but for both the separation between the wires is around 1 mm. All of the sensors except the $l_w = 1$ mm XW are based on Dantec probes modified to use in-house etched platinum-(10 %) rhodium Wollaston wires soldered to the prongs (further details can be found in table 2). The $l_w = 1$ mm XW is a Dantec 55P51 tungsten probe. It should be noted that the $l_w = 0.2$ mm SW, which has a diameter of $d_w = 1.27$ μm, is operated in the limit of the bridge stability, on the verge of having non-damped oscillations. Nonetheless, the sine-wave test indicated that $f_{cut\text{-}off}^{0\ \mathrm{dB}}$ was about 40 kHz. The hot wires are calibrated at the beginning and at the end of each measurement campaign using a fourth-order polynomial in the SW case and a velocity-pitch map in the XW case. Note that, unless otherwise stated, the data shown are acquired with the $l_w \approx 1$ mm SW hot-wire probe. All of the two-component data presented are acquired with the $l_w \approx 0.5$ mm XW except the spanwise traverse data presented in § 3.2.1.

Note that two other anemometry systems have been used as well in order to allow a comparison with previous experimental results, but these results are not included here. The other anemometry systems are the AALab AN-1005 CTA system used in Seoud & Vassilicos (2007) and Hurst & Vassilicos (2007) and the DISA 55M10 CTA bridge with a DISA 55D26 signal conditioner used in Mazellier & Vassilicos (2010). It is found that the results obtained with the DISA 55M10 CTA unit closely match those obtained with the StreamLine CTA system, when the same hot-wire probe is used, except at very high frequencies where the higher noise floor of the DISA CTA system buries the velocity signal. On the other hand it is found that the measurements taken with the AALab AN-1005 CTA system are significantly different at frequencies above 6 kHz and therefore the turbulence statistics involving velocity derivatives are significantly different. This is likely the reason for the difference between the normalized energy dissipation rate C_ε results reported in Seoud & Vassilicos (2007)

SW/XW	l_w (mm)	d_w (μm)	l_w/d_w	Hot-wire probe	U_∞ (m s^{-1})	$f_{cut\text{-}off}^{-3\ \mathrm{dB}}$ (kHz)	$f_{cut\text{-}off}^{0\ \mathrm{dB}}$ (kHz)	l_w/η
SW	~ 1	5.1	196	55P16	10	~ 25	~ 12	7–3
					15	~ 32	~ 16	9–5
SW	~ 0.45	2.5	180	55P16	10	~ 45	~ 21	3–2
					15	~ 45	~ 23	4–2
SW	~ 0.2	1.27	157	55P11	10	> 50	~ 40	~ 1
					15	> 50	~ 40	2–1
XW	~ 0.5	2.5	200	55P51	10	~ 45	~ 21	3–2
					15	~ 45	~ 23	4–2
XW	1.0	5	200	55P51	15	~ 30	~ 14	9–5

TABLE 2. Details of the hot wires, cut-off frequencies and resolution. Here l_w and d_w are the sensing length and diameter of the wires, l_w/η is the ratio between the sensing length and the Kolmogorov inner length scale, U_∞ is the inlet velocity, $f_{cut\text{-}off}^{-3\ \mathrm{dB}}$ is the cut-off frequency corresponding to -3 dB signal attenuation and $f_{cut\text{-}off}^{0\ \mathrm{dB}}$ is the highest frequency with negligible attenuation.

Grid	N	L_0 (mm)	t_0 (mm)	L_r	t_r	R_L	R_t	σ	M_{eff} (mm)
FSG	4	237.8	19.2	8	17	0.5	2.57	0.25	26.2
RG	1	60	10	1	1	1	1	0.32	60

TABLE 3. Details of the RG and the low-blockage space-filling FSG. Here N is the number of fractal iterations of the grids (for a RG $N = 1$), L_0 is the centreline distance separating the largest bars and t_0 their lateral thickness, see figure 1, L_r and t_r are respectively the length and thickness ratio between the largest and smallest bars, R_L and R_t are the length and thickness ratio between two consecutive fractal iterations and R_t is related to t_r and N via $t_r = R_t^{-N+1}$. The blockage ratio σ is defined as the fraction of area occupied by the grid and M_{eff} is the effective mesh size as defined in Hurst & Vassilicos (2007) which reverts to the definition of mesh size for a RG.

and the ones presented in § 3.3 of this paper. The comparison between the results of the different anemometry systems will be presented elsewhere.

2.2. *Data acquisition and signal processing*

The pressure and temperature measurements are digitally transferred to the computer using a parallel port. The analogue signal from the anemometers is sampled using a 16-bit National Instruments NI-6229 (USB) card, at a sampling frequency set to be higher than twice the analogue low-pass filtering frequency (30 kHz). The data acquisition and signal processing are performed with the commercial software MATLAB™.

The turbulent velocity signal was acquired for 9 min corresponding to more than 100 000 integral-time scales. This was confirmed to be sufficient for converged measured statistics of interest such as the integral scale, the first four moments of the velocity signal and the second moment of the velocity derivative signal. The time-varying turbulent signal was converted into spatially varying by means of a local Taylor's hypothesis following the algorithm proposed in Kahalerras *et al.* (1998). Before Taylor's hypothesis is used the signal is digitally filtered at a frequency

corresponding to $k_1\eta \sim 1.1$ (where $\eta \equiv (\nu^3/\varepsilon)^{1/4}$ is the Kolmogorov inner length scale and k_1 the wavenumber) using a fourth-order Butterworth filter to eliminate higher-frequency noise.

The integral scale L_u is estimated as

$$L_u = \int_0^{r_L} f(r)\,\mathrm{d}r, \tag{2.1}$$

where $f(r) \equiv \overline{u(x)u(x+r)}/\overline{u(x)^2}$ is the auto-correlation function of the streamwise velocity fluctuations for streamwise separations r and r_L is maximum integration range taken to be about 10 times the integral length scale. It was checked that (i) changing the integration limit r_L by a factor between 2/3 and 2 has little effect on the numerical value of the integral scale and (ii) the choice of r_L, if large enough, does not influence the way that L_u varies with downstream distance. The transverse integral scale is estimated in a similar way. The longitudinal and transverse spectra are calculated using a fast Fourier transform (FFT)-based periodogram algorithm using a Hanning window with 50 % overlap and window length equivalent to at least 180 integral length scales. The dissipation ε is estimated from the longitudinal wavenumber spectra F_{11} as

$$\varepsilon = 15\nu \int_{k_{min}}^{k_{max}} k_1^2 F_{11}(k_1)\,\mathrm{d}k_1, \tag{2.2}$$

where k_{min} and k_{max} are determined by the window length and the sampling frequency, respectively. To reduce the unavoidable contamination of noise at high frequencies (which can bias the dissipation estimate) we follow Antonia (2003) and fit an exponential curve to the high-frequency end of the spectra which we then integrate. We checked that calculating the dissipation with and without Antonia's (2003) method changes the dissipation by less than 4 % in the worst case.

It might be worth mentioning that the measurements of the fractal-grid-generated turbulence posed less of a challenge to hot-wire anemometry than the RG-generated turbulence quite simply because the turbulent signal to anemometry noise ratio is higher in the former case, but nonetheless the Kolmogorov microscales (which influence the maximum frequency to be measured) for the highest Re_λ measurement location ($Re_\lambda \approx 350$ and $Re_\lambda \approx 150$, respectively) are roughly the same ($\eta \approx 0.11$ mm and $\eta \approx 0.13$ mm respectively).

2.3. *Turbulence-generating grids*

The bulk part of the measurements are performed on turbulence generated by a low-blockage space-filling FSG with four 'fractal iterations' and a thickness ratio of $t_r = 17$, see figure 1. It is one of the grids used in the experimental setup of Mazellier & Vassilicos (2010) where further details of the fractal grids and their design can be found. Measurements of turbulence generated by a bi-plane RG with a square mesh and composed of square rods are also performed. The summary of the relevant grid design parameters is given in table 3.

3. Results

The turbulent field in the lee of the space-filling FSGs can be considered to have two distinct regions (Hurst & Vassilicos 2007; Mazellier & Vassilicos 2010): a production region where the turbulent kinetic energy (on the centreline) is increasing and the flow is being homogenized, and a decay region where the energy of the turbulent fluctuations are rapidly decreasing and the flow is roughly homogeneous with

an isotropy factor around $u'/v' \sim 1.1$–1.25, where u' and v' are the longitudinal and transverse r.m.s. velocities, respectively.

3.1. *The wake-interaction length scale*

Mazellier & Vassilicos (2010) introduced the wake-interaction length scale $x_* = L_0^2/t_0$ (see definitions of L_0 and t_0 in figure 1 and in the caption of table 3) to characterize the extent of the turbulence production region in the lee of the FSGs. This length scale is based on the largest square of the grid since the wakes it generates are the last to interact, although there is a characteristic wake-interaction length scale for each grid iteration (for a schematic of the wake interactions occurring at different streamwise locations refer to figure 4(*a*) in Mazellier & Vassilicos 2010). They then related the wake-interaction length scale with the location of the maximum of the turbulence intensity along the centreline x_{peak}, which marks the end of the production region and the start of the decay region and found that $x_{peak}/x_* \approx 0.45$. Note that this is not the only peak in turbulence intensity in the domain nor is it the overall maximum, but it is the last peak occurring furthest downstream before decay. This can be seen for example in figure 9 in Mazellier & Vassilicos (2010), where the streamwise variations of the turbulence intensity both along the centreline and along an off-centre parallel line are shown. The turbulence intensity along this particular off-centre line peaks much closer to the grid and at a higher-intensity value than the turbulence recorded on the centreline.

The wake-interaction length scale can also be defined for a RG, where the mesh size and the bar thickness are now the relevant parameters, $x_* = M^2/t_0$. Jayesh & Warhaft (1992) measured the turbulence intensity very near the grid, $1 < x/M < 30$ and observed two different regions, a highly inhomogeneous region up to $x/M \approx 3$ which is a production region where the turbulence intensity increases along a streamwise line crossing half the distance between grid bars and a decay region beyond that. Note that $x/M \approx 3$ corresponds to $x_{peak}/x_* \approx 0.55$ close to $x_{peak}/x_* \approx 0.45$ encountered by Mazellier & Vassilicos (2010) for the FSGs. A qualitatively similar conclusion can be drawn from the DNS of turbulence generated by a RG presented in Ertunç *et al.* (2010). In their figure 16 one can find the development of the turbulent kinetic energy very close to the grid $0.5 < x/M < 10$ along three straight streamwise lines located, respectively, behind a grid bar, half the distance between bars and in between the other two traverses. It can be seen that the turbulence intensity peaks first directly behind the grid bar at $x_{peak}/M \approx 1$ and lastly behind the half-distance between grid bars (somewhat equivalent to the centreline in the FSG) at $x_{peak}/M \approx 2.5$. This latter streamwise location corresponds to $x_{peak}/x_* \approx 0.68$, once more not far from $x_{peak}/x_* \approx 0.45$. Note nonetheless that this simulation was performed at very low Reynolds numbers, $Re_\lambda < 17$, so care must be taken in quantitative comparisons.

Note that x_{peak}/x_* appears to be slightly higher for the static RGs than for the FSGs. This is likely due not only to the typically low Reynolds numbers generated by the RGs, but also to the characteristic production mechanism of the FSGs, i.e. before the larger wakes interact all of the smaller wakes have already interacted and generated turbulence that increases the growth rate of the larger wakes, thus making them meet closer to the grid and therefore causing a smaller value of x_{peak}/x_*.

The fact that the fractal grid has multiple wake-interaction length scales, for the present FSG ranging from a few centimetres to more than a metre, is precisely part of what makes the fractal grid generate turbulence that is qualitatively different from RG-generated turbulence. Consequently one could expect that a fractal grid designed so that it produces a narrow range or a single dominant wake-interaction length scale,

will lead to turbulence that is similar to RG-generated turbulence. Hurst & Vassilicos (2007) included the assessment of fractal cross grids in their study, which resemble RGs but with bars of varying thicknesses. The ratios between the thickest and the thinnest bars of their fractal cross grids ranged from 2.0 to 3.3, thus yielding a narrow span of wake-interaction length scales. Furthermore, the wake-interaction pattern of the fractal cross grids, as designed and studied in Hurst & Vassilicos (2007), is considerably different from the wake-interaction pattern of their FSGs. In the FSG case, the main interaction events occur when similar sized wakes meet, whereas in the fractal cross grids the main interaction events occur between adjacent wakes, which may or may not be of similar size. Therefore, one could expect the results obtained with fractal cross grids, for example the power-law turbulence decay exponent, to be somewhat similar the typical results found for RG-generated turbulence. In fact, examining figure 10 in Hurst & Vassilicos (2007) one can see that the turbulence decays as $(x - x_0)^{-n}$ with $1 < n < 1.5$ for $x_0 \approx 0$, although they encounter a general difficulty of finding the appropriate virtual origin. We return to the problem of finding the appropriate virtual origin and the power-law decay exponent in § 3.4 where we present different power-law decay fitting methods applied to our data.

3.2. *Homogeneity, isotropy and wall interference*

3.2.1. *Homogeneity*

Previous experimental investigations on the turbulence generated by space-filling FSGs (e.g. Mazellier & Vassilicos 2010) reported that the flow field close to the grid is highly inhomogeneous. It was also observed that during the process of turbulent kinetic energy build up, the turbulent flow is simultaneously homogenized by turbulent diffusion, and by the time it reaches a peak in turbulence intensity (what they considered to be the threshold between the production and decay regions) the flow has smoothed out most inhomogeneities. Seoud & Vassilicos (2007) measured the turbulent kinetic energy production in various planes perpendicular to the mean flow along the centreline and observed that the turbulent production decreases rapidly just after the peak, i.e. where $0.45(\approx x_{peak}/x_*) < x/x_* < 0.75$ and that the turbulent energy production typically represents less than 30 % of the dissipation and never exceeds 20 % beyond this region.

Mazellier & Vassilicos (2010) compared the characteristic time scales of the mean velocity gradients $(\partial U/\partial x)^{-1}$ and $(\partial U/\partial y)^{-1}$ (where U is the streamwise mean velocity and y is a coordinate along the horizontal normal to the streamwise direction) with the time scale associated with the energy-containing eddies and reached the conclusion that beyond the peak the mean gradient time scale is typically one to two orders of magnitude larger. Consequently the small-scale turbulence dynamics are not affected by large-scale mean flow inhomogeneities.

Here we complement the previous analyses by following the approach of Corrsin (1963) and Comte-Bellot & Corrsin (1966) and using some of their homogeneity criteria, as they did for RGs. The commonly accepted 'rule-of-thumb' for the RGs is that the turbulent flow can be considered statistically homogeneous in transverse planes for $x/M > 30$ and the unavoidable inhomogeneity along the mean flow direction becomes relatively unimportant for $x/M > 40$ (Corrsin 1963).

For the downstream decaying turbulence to be considered a good approximation to spatially homogeneous decaying turbulence, two criteria must be met: (i) the eddy turnover time L_u/u' must be small compared with the time scale associated with the velocity fluctuation decay rate $(\partial u'/\partial x)^{-1}$ (see also § 3.3 of Townsend 1956); and (ii) the rate of change of the turbulent length scales must be small compared with the

length scales themselves. Following Corrsin (1963) we measure

$$\frac{L_u}{\overline{u^2}}\frac{\partial \overline{u^2}}{\partial x}, \quad \frac{L_u}{\lambda}\frac{\partial \lambda}{\partial x}, \quad \frac{\partial L_u}{\partial x}, \tag{3.1}$$

and confirm that these quantities are small for the entire decay region assessed here, i.e. $x/x_* > 0.6$ (figure 2*a*) and comparable with those obtained for a RG (figure 2*b*). Note that the 'rule-of-thumb' $x/M > 40$ suggested by Corrsin (1963) was based on the streamwise location where his RG data yielded these dimensionless quantities to be below 4 %, so for our RG data this 'rule-of-thumb' translates to $x/M > 25$ and for our FSG data to $x/x_* > 0.7$.

A thorough assessment of the inhomogeneity of the flow can be made by using the statistical equations and measuring the terms that should be zero in a statistically homogeneous flow field. Starting with single-point statistics, e.g. the turbulent kinetic energy equation (here $U_1 = U$, $U_2 = V$ and $U_3 = W$ denote mean flow speeds, $u_1 = u$, $u_2 = v$, $u_3 = w$ and p are zero mean fluctuating velocities and pressure, and $x_1 = x$, $x_2 = y$ and $x_3 = z$ are the components of a coordinate system aligned with the respective velocity components),

$$\frac{U_k}{2}\frac{\partial \overline{q^2}}{\partial x_k} = -\overline{u_i u_j}\frac{\partial U_i}{\partial x_j} - \frac{\partial}{\partial x_k}\left(\frac{\overline{u_k q^2}}{2} + \frac{\overline{u_k p}}{\rho}\right) + \frac{\nu}{2}\frac{\partial^2 \overline{q^2}}{\partial x_m \partial x_m} - \nu\overline{\frac{\partial u_i}{\partial x_k}\frac{\partial u_i}{\partial x_k}}, \tag{3.2}$$

where use is made of Einstein's notation and $\overline{q^2} \equiv \overline{u^2} + \overline{v^2} + \overline{w^2}$ ($K \equiv \frac{1}{2}\overline{q^2}$), overbars signifying averages over an infinite number of realizations (here, over time).

The flow statistics inherit the grid symmetries, i.e. reflection symmetry around the y- and z-axes (as well as diagonal reflection symmetry) and symmetry with respect to discrete 90° rotations and therefore the transverse mean velocities are negligibly small, $V = W \approx 0$, and the turbulent kinetic energy equation at the centreline reduces to

$$\frac{U}{2}\frac{\partial \overline{q^2}}{\partial x} = \overbrace{-\left(\overline{u^2}\frac{\partial U}{\partial x} + 2\overline{uv}\frac{\partial U}{\partial y}\right)}^{\mathscr{P}} \overbrace{-\left(\frac{\partial}{\partial x}\frac{\overline{uq^2}}{2} + 2\frac{\partial}{\partial y}\frac{\overline{vq^2}}{2}\right)}^{\mathscr{T}}$$
$$\underbrace{-\left(\frac{\partial}{\partial x}\frac{\overline{up}}{\rho} + 2\frac{\partial}{\partial y}\frac{\overline{vp}}{\rho}\right)}_{\Pi} \underbrace{+\frac{\nu}{2}\left(\frac{\partial^2 \overline{q^2}}{\partial x^2} + 2\frac{\partial^2 \overline{q^2}}{\partial y^2}\right)}_{\mathscr{D}_\nu} \underbrace{-\nu\overline{\frac{\partial u_i}{\partial x_k}\frac{\partial u_i}{\partial x_k}}}_{\varepsilon}, \tag{3.3}$$

where $\mathscr{P}$, $\mathscr{T}$, Π, $\mathscr{D}_\nu$ and ε are the production, triple-correlation transport, pressure transport, viscous diffusion and dissipation terms, respectively.

Data from both single- and cross-wire measurements are used to estimate all of the terms in (3.3) (except the pressure–velocity correlations) along the centreline in the decay region for $U_\infty = 15$ m s^{-1} (see table 4). The pressure transport is indirectly estimated from the balance of (3.3). The last term in (3.3) is evaluated assuming isotropy: for the SW measurements $\varepsilon_{iso}^{SW} \equiv 15\nu\overline{(\partial u/\partial x)}$; for the XW measurements one can impose one less isotropy constraint and estimate ε from $\varepsilon_{iso}^{XW} \equiv 3\nu\overline{(\partial u/\partial x)} + 6\nu\overline{(\partial v/\partial x)}$ (Schedvin, Stegen & Gibson 1974). It should be noted that the separation between the XWs is about 1 mm and is almost 10 times the Kolmogorov length scale so caution should be taken interpreting the direct measurements of dissipation using the XWs as they may be underestimated. On the

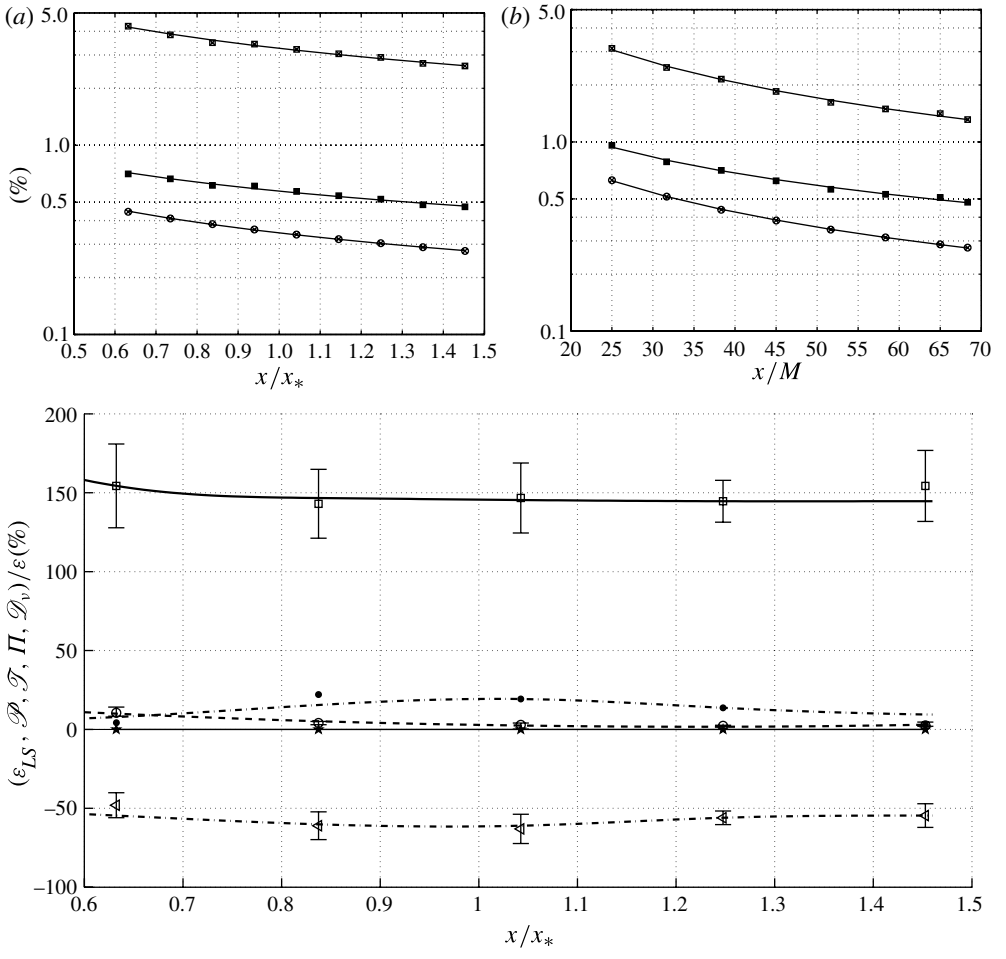

FIGURE 2. Homogeneity assessment for the FSG in the decay region around the centreline for $U_\infty = 15\ \mathrm{m\ s^{-1}}$. Top figures: dimensionless streamwise inhomogeneity measures (⊠) $(L_u/\overline{u^2})(\partial\overline{u^2}/\partial x)$, (■) $(L_u/\lambda)(\partial\lambda/\partial x)$, (⊗) $(\partial L_u/\partial x)$ for the (*a*) FSG, (*b*) RG. Bottom figure: (*c*) turbulent kinetic energy budget (3.3) normalized by the dissipation for the FSG at the centreline, (□) ε_{LS} – advection, (○) $\mathscr{P}$ – production, (◁) $\mathscr{T}$ – triple-correlation transport, (●) Π – pressure transport, (⋆) $\mathscr{D}_v$ – viscous diffusion.

other hand the isotropic estimate of the dissipation using SW measurements is likely to be overestimated since we show that $\overline{(\mathrm{d}v/\mathrm{d}x)^2}/\overline{(\mathrm{d}v/\mathrm{d}x)^2} < 2$. In figure 2(*c*) the mean between the SW and XW dissipation estimates is used as the normalizing quantity and the error (taken as the difference between the two estimates) contributes to the error bar of the normalized quantities. The advection $1/2\,U\partial\overline{q^2}/\partial x$ is estimated from the nonlinear least-squares power law fit of $\overline{q^2}$ (see § 3.4 for further details) and $\overline{q^2}$ is estimated as $\overline{q^2} = \overline{u^2}(1 + 2\overline{v^2}/\overline{u^2})$ with $\overline{u^2}$ from the SW data and $\overline{v^2}/\overline{u^2}$ from the XW data; for the advection as well, the error is taken to be the difference between the SW (no anisotropy correction) and XW estimate. The ratio between advection and dissipation can be seen (figure 2*c*) not to be unity but tending to be approximately 1.5 beyond $x/x_* \approx 0.8$; we return to this issue at the end of this section and in § 3.4 where we estimate the decay rate of our turbulence.

Position (mm)	1850	2450	3050	3650	4250
x/x_*	0.63	0.83	1.04	1.24	1.44
Re_λ	352	292	253	226	210
$\sqrt{\overline{u^2}}$ (m s^{-1})	1.28	0.99	0.79	0.65	0.56
L_u (mm)	45.7	47.6	50.0	50.7	53.6
λ (mm)	4.1	4.4	4.8	5.2	5.6
η (mm)	0.11	0.13	0.15	0.18	0.2
$\varepsilon_{LS} \equiv -(U/2)(\partial/\partial x)\overline{u^2}\left(1+2(\overline{v^2}/\overline{u^2})\right)$ (m^2 s^{-3})	28.6	13.9	7.7	4.7	3.0
$\varepsilon_{iso}^{SW} \equiv 15\nu\overline{(\partial u/\partial x)^2}$ (m^2 s^{-3})	21.6	11.1	6.0	3.5	2.2
$\varepsilon_{iso}^{XW} \equiv 3\nu\overline{(\partial u/\partial x)^2} + 6\nu\overline{(\partial v/\partial x)^2}$ (m^2 s^{-3})	16.6	8.7	4.7	3.1	1.7
$-\overline{u^2}(\partial U/\partial x)$ (m^2 s^{-3})	0.62	0.27	0.11	0.07	0.05
$-2\overline{uv}(\partial U/\partial y)$ (m^2 s^{-3})	1.32	0.12	0.04	0.004	0.0007
$(\partial/\partial x)(\overline{uq^2}/2)$ (m^2 s^{-3})	0.69	0.39	0.06	−0.01	−0.004
$2(\partial/\partial y)(\overline{vq^2}/2)$ (m^2 s^{-3})	8.22	5.53	3.25	1.83	1.08
$\nu(\partial^2\overline{q^2}/\partial x^2)$ ($\times 10^5$)(m^2 s^{-3})	4.23	1.72	0.81	0.42	0.024
$-\nu(\partial^2\overline{q^2}/\partial y^2)$ ($\times 10^3$)(m^2 s^{-3})	3.24	1.55	1.29	1.08	0.45
$\sqrt{\overline{u^2}/\overline{v^2}}$	1.15	1.13	1.11	1.13	1.10
$\overline{(\mathrm{d}v/\mathrm{d}x)^2}/\overline{(\mathrm{d}u/\mathrm{d}x)^2}$	1.39	1.40	1.42	1.44	1.46
L_u/L_v	3.7	3.2	3.0	2.7	3.0

TABLE 4. Turbulence statistics for five streamwise locations recorded at $U_\infty = 15$ m s^{-1}.

The longitudinal production terms are calculated from the SW data (finer streamwise resolution), whereas the transverse production terms are estimated using the XW spanwise traverse data. The latter contribution $\overline{uv}\,\partial U/\partial y$ is approximately zero at the centreline (due to the reflexion symmetry), so it is preferred to estimate it just off the centreline around $y \pm 10$ mm $\approx L_u/5 \approx L_v/2$, to infer on its contribution in this region of the flow. The total contribution from the production terms around the centreline can be seen (figure 2*c*) to be less than 10 % of the estimated dissipation (in agreement with Seoud & Vassilicos 2007) and beyond $x > x_*$ they become negligible (there is a residual production of 2–4 % of the dissipation due to non-vanishing streamwise mean velocity gradients). The viscous diffusion, as expected, is always negligibly small (table 4). The longitudinal triple-correlation transport (table 4) shows a trend not dissimilar to that of the production terms, it is less than 10 % closer to the kinetic energy peak ($x/x_* < 0.8$) and becomes vanishingly small beyond $x > x_*$.

The transverse triple-correlation transport was assessed by measuring the triple correlation $\overline{vq^2}/2$ (figure 3*a*) along the vertical symmetry plane of the grid ($z = 0$) for the five streamwise downstream locations specified in table 4. The transverse measurements ranged from the lower to the upper largest bars of the fractal grid (-120 mm $< y <$ 120 mm) and were recorded with a spacing of 20 mm. The total transverse triple-correlation transport $\mathrm{d}\overline{vq^2}/\mathrm{d}y$ (i.e. twice the transport at each transverse direction y and z) decreases together with the dissipation and not faster as

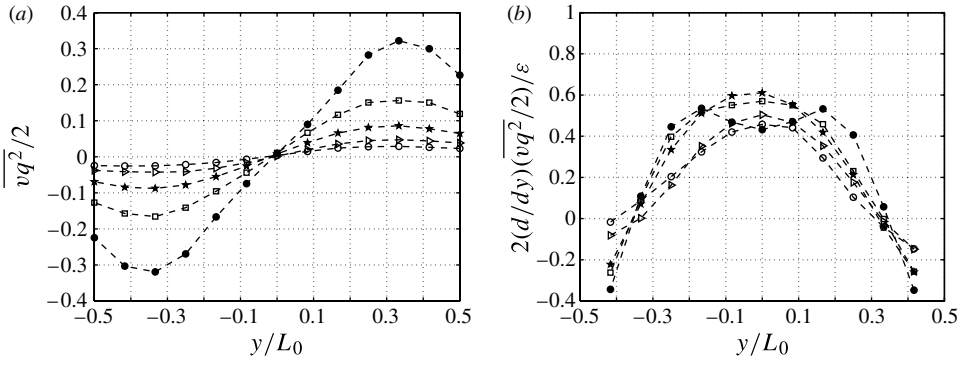

FIGURE 3. Transverse profiles of (*a*) $(\overline{vq^2}/2)$, (*b*) $2(\mathrm{d}/\mathrm{dy})(\overline{vq^2}/2)/\varepsilon$ at five streamwise downstream positions and $U_\infty = 15\ \mathrm{m\ s^{-1}}$: (●) $x/x_\star = 0.63$, (□) $x/x_\star = 0.83$, (⋆) $x/x_\star = 1.04$, (▷) $x/x_\star = 1.24$, (○) $x/x_\star = 1.44$.

the other measured inhomogeneity terms (figure 2*c*). It typically amounts to 40–60 % of the dissipation (at the centreline) and perhaps surprisingly, it stays nearly the same fraction for the entire decay region assessed. This seems to be the case not only along the centreline but for all of the transverse measurement locations as well (figure 3*b*), although the ratio between the transport and dissipation are different for different y locations and can if fact be zero or negative (at $y/L_0 \approx 0.35$ and beyond that respectively).

In § 3.4 we argue that this persistent spanwise energy transport has no significant effect on the power law exponent of the turbulence energy decay because the dissipation and the lateral transport remain roughly proportional throughout the part of the decay region explored here.

3.2.2. *Isotropy*

The simplest assessment of large-scale anisotropy is achieved by comparing the ratio of streamwise and transverse r.m.s. velocity components, sometimes referred to as an isotropy factor. The results of such measurements at the centreline are presented in table 4 and show a fair agreement with Hurst & Vassilicos (2007) for the same set-up, confirming that the flow is reasonably isotropic for the entire decay region assessed, $u'/v' \approx 1.1$–1.25. The range of isotropy factors encountered in our flow are comparable with those obtained by Mydlarski & Warhaft (1996) for their active grids, although further research shows it is possible to tune the active grid to decrease the anisotropy of the flow (Kang, Chester & Meneveau 2003). Similarly it should be possible to further optimize the design of the fractal grids to increase isotropy, e.g. by increasing the thickness ratio as is suggested by the data presented by Hurst & Vassilicos (2007). Hurst & Vassilicos (2007) also reported the ratio between the longitudinal and transversal integral length scales (L_u and L_v) for the same low-blockage space-filling FSG to be $L_u/L_v \approx 2$, but this is not confirmed by the present data where the integral scales ratio is larger than 2 as shown in table 4, even though this ratio decreases further downstream. This discrepancy is likely due to the calculation method of the transversal integral scales; integrating the transverse correlation function to the first zero crossing as Hurst & Vassilicos (2007) (incorrectly) did we recover an integral scale ratio closer to 2.

A complementary assessment of isotropy is obtained by computing the longitudinal and transversal correlation functions, $f(r,x) \equiv \overline{u(x)u(x+r)}/\overline{u(x)^2}$ and $g(r,x) \equiv$

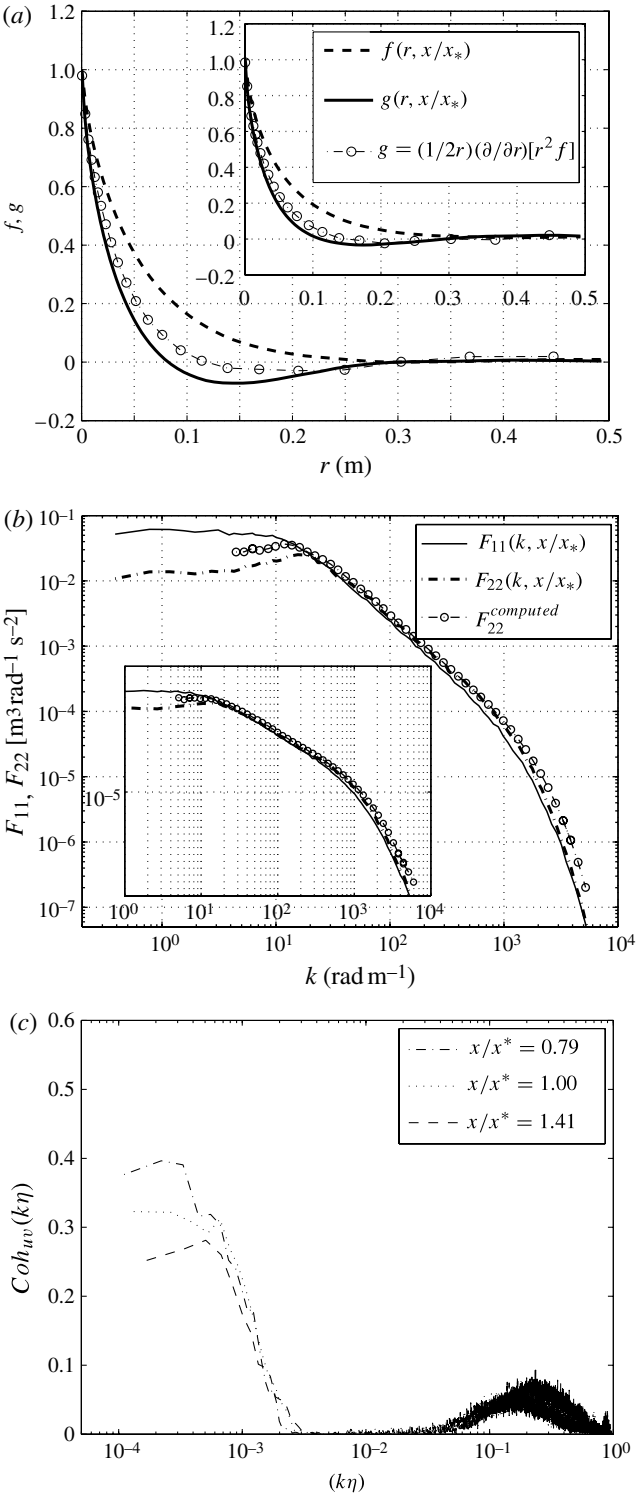

FIGURE 4. Longitudinal and transversal one-dimensional (*a*) correlation function, (*b*) energy spectra for $x/x_* = 0.63$ (and for $x/x_* = 1.4$ in the insert) and (*c*) coherence spectra in the coordinate system rotated 45° with respect to the flow direction. Here $U_\infty = 15$ m s^{-1}.

$\overline{v(x)v(x+r)}/\overline{v(x)^2}$, and comparing $g(r,x)$ with $g^{iso}(r) = (1/2r)\,\mathrm{d}[r^2 f(r)]/\mathrm{d}r$ which is the relation between the two correlation functions in the presence of isotropy. The comparison is shown in figure 4(*a*) for two downstream locations and it can be seen that there is a modest agreement between the measured and computed transverse correlation functions, although the agreement improves downstream. A similar comparison in spectral space is shown in figure 4(*b*), where the isotropic relation between the longitudinal and transversal one-dimensional spectra is $F_{22}^{iso} = [F_{11} + k_1\,\mathrm{d}F_{11}/\mathrm{d}k_1]/2$. There is a fair agreement between the measured and computed transverse one-dimensional spectra in the 'inertial region', but not at the low wavenumbers (which is consistent with $L_u/L_v > 2$) nor at high wavenumbers (reflecting that $\overline{(\mathrm{d}v/\mathrm{d}x)^2}/\overline{(\mathrm{d}u/\mathrm{d}x)^2} < 2$). This lack of small-scale isotropy was not reported by Seoud & Vassilicos (2007) nor by Mydlarski & Warhaft (1996) in their active-grid experiments because they filtered out the highest frequencies where their XW measurements could not be trusted. Note that in agreement with the latter experiments the coherence spectra (figure 4*c*) show that the anisotropy (inferred by the cross-correlation of the velocity components in a coordinate system rotated by 45°) is mostly contained in the large scales. The cause for this, perhaps apparent, small-scale anisotropy in figure 4 and in our values of $\overline{(\mathrm{d}v/\mathrm{d}x)^2}/\overline{(\mathrm{d}u/\mathrm{d}x)^2}$ in table 4, is most probably the separation between the XWs (≈ 1 mm) being up to 10 times the Kolmogorov length scale. It should be noted that, precisely because of this problem, the velocity derivative ratios in Seoud & Vassilicos (2007) were obtained for a low-pass filtered velocity signal at $k\eta \approx 0.1$. In this way, these authors obtained $\overline{(\mathrm{d}v/\mathrm{d}x)^2}/\overline{(\mathrm{d}u/\mathrm{d}x)^2} \simeq 2$ even though strictly speaking $\overline{(\mathrm{d}u_i/\mathrm{d}x)^2} = \int_0^\infty k_1^2 F_{ii}(k_1)\,\mathrm{d}k_1$, where contributions coming from $k\eta > 10^{-1}$ cannot necessarily be written off as negligible.

3.2.3. *Wind-tunnel confinement*

A qualitative assessment of the effect of flow confinement in wind-tunnel experiments can be made by comparing the tunnel's height/width with the flow's integral scale and comparing the ratio with similar experiments and with DNSs. For simplicity we take the longitudinal integral scale at the centreline to be the representative scale for each transverse section and it is typically 8.5 to 10 times smaller than the wind-tunnel width (for an isotropic flow the longitudinal integral scale and that obtained using the three-dimensional energy spectrum $L = \pi/\overline{u^2}\int_0^\infty E(k,t)/k\,\mathrm{d}k$ coincide). This is just about in-line with what is typically used in the DNS of decaying homogeneous turbulence Ishida, Davidson & Kaneda (2006) and Wang & George (2002), considering the boundary layers on the walls of the wind tunnel which reduce the effective transverse size of the tunnel down to eight times the integral scale (based on the displacement thickness of the boundary layers) very far downstream. The active-grid experiments by Mydlarski & Warhaft (1996) were performed at equivalent Re_λ in a similar sized wind tunnel and produced larger integral scales but were in line with typical decay properties and did not observe any of the outstanding features of our flow reported in the §§ 3.3, 3.4 and 3.5. (Note that Mydlarski & Warhaft (1996) used a different definition of integral scale, but Gamard & George (2000) used the same data to extract the integral scale as defined here.) It is therefore unlikely that our results, namely the abnormally high decay exponent and the proportionality between the integral and the Taylor microscale, may be due to confinement. However, it is conceivable that the effective choking of the tunnel by the growing boundary layers very far downstream does have some effect on the larger turbulence scales at these very far distances (see figure 5).

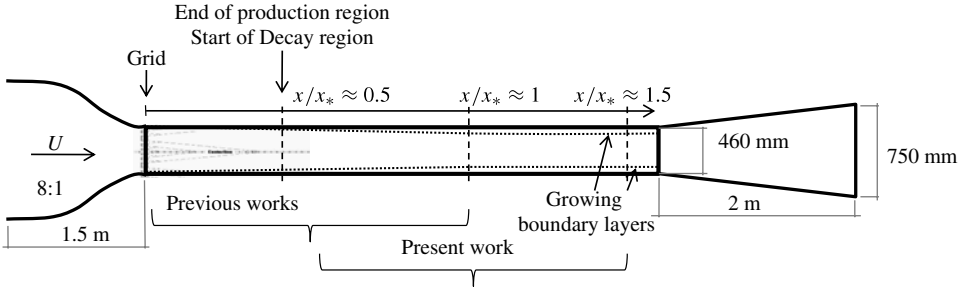

FIGURE 5. Sketch of the wind tunnel where the decay of turbulence generated by regular and fractal square grids was measured. This wind tunnel is a modified version, with an extended test section, of the wind tunnel used by Hurst & Vassilicos (2007), Seoud & Vassilicos (2007) and Mazellier & Vassilicos (2010) in their experimental investigations of fractal generated turbulence. The boundary layers developing at the wall were estimated to have a displacement thickness of $\delta_1 \approx 4$ mm at $x = 2$ m ($x/x_* = 0.7$), $\delta_1 \approx 8$ mm at $x = 3.5$ m ($x/x_* = 1.2$) and $\delta_1 \approx 10$ mm at $x = 4.5$ m ($x/x_* = 1.5$).

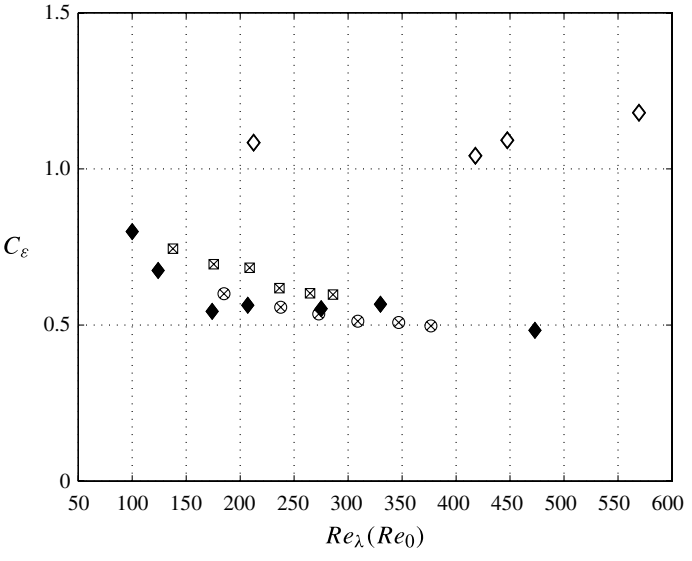

FIGURE 6. Normalized energy dissipation rate C_ε versus Re_λ with Re_λ changing as a function of the inlet Reynolds number Re_0 for a fixed streamwise downstream location for turbulence generated from fractal square grids (FSGs), active grids and regular grids (RGs). For the FSG data the inlet Reynolds number is changed by varying the free stream speed between 5 m s^{-1} $< U_\infty <$ 17.5 m s^{-1} and is measured with a $l_w = 0.45$ mm sensing length SW at two streamwise downstream positions: (⊗) $x/x_* = 0.63$ and (⊠) $x/x_* = 1.04$. (♦) Active-grid data is taken from table 1 of Gamard & George (2000) which is based on the experimental data by Mydlarski & Warhaft (1996) (Gamard & George 2000 computed the longitudinal and the transverse integral scales from the spectra, but their latter estimate yielded less scatter, hence we assume isotropy and use twice the transverse integral scale). (◊) RG data from the data compilation by Sreenivasan (1984, figure 1) (only data by Kistler & Vrebalovich 1966 is used since no other experiment with more than one data point had $Re_\lambda > 100$).

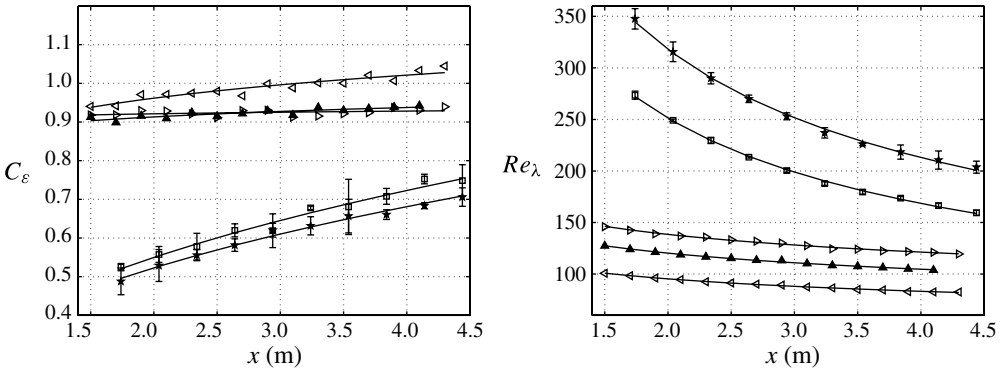

FIGURE 7. Normalized energy dissipation rate C_ε and Reynolds number Re_λ versus streamwise downstream location x for both the FSG and RG data recorded at different inlet velocities: (□) FSG at $U_\infty = 10$ m s^{-1}, (⋆) FSG at $U_\infty = 15$ m s^{-1}, (◁) RG at $U_\infty = 10$ m s^{-1}, (▲) RG at $U_\infty = 15$ m s^{-1}, (▷) RG at $U_\infty = 20$ m s^{-1}. Since the FSG data is acquired with three different wire resolutions (see § 2.1) we plot the arithmetic mean plus error bars.

3.3. *Normalized energy dissipation rate*

It follows from this paper's introduction that for fully developed turbulence generated by at least some space-filling low blockage FSGs, the normalized energy dissipation rate C_ε depends both on an initial conditions/global Reynolds number Re_0 (e.g. $Re_0 \equiv U_\infty x_*/\nu$) and on a local Reynolds number ($Re_\lambda(x)$). This distinction between two different Reynolds number dependencies follows from (1.5) and (1.7) and does not need to be made in the context of the Richardson–Kolmogorov phenomenology where the functions A and B are identical and the exponents α and β are both equal to $1/2$.

The present measurements of the normalized energy dissipation rate C_ε for different Re_0 (by varying U_∞) at two fixed streamwise downstream positions from the fractal grid (figure 6) suggest that $C_\varepsilon(Re_0)$ is roughly constant beyond $Re_\lambda(Re_0) \approx 200$ (figure 6). From (1.7), this observation implies that, at high enough values of Re_0, $\alpha = \beta$ and

$$C_\varepsilon = 15A\left(\frac{x - x_0}{x_*}\right) \Big/ B\left(\frac{x - x_0}{x_*}\right) \tag{3.4}$$

irrespective of Re_0. The facts that A is a slow-varying function whereas B is a fast-varying function of $(x - x_0)/x_*$ is reflected in the steep increase of C_ε with x (see figure 7*a*). This is fundamentally different from the cornerstone assumption that C_ε is constant, an assumption which is approximately verified by the turbulence generated by our RG provided Re_0 is large enough (see figure 7*a*).

The high Re_0 behaviour of $C_\varepsilon(Re_0)$ is very comparable to that found with RGs and active grids at similar Reynolds numbers (figure 6) and more generally with other boundary-free turbulent flows such as various wakes (see e.g. Burattini *et al.* 2005; Pearson, Krogstad & van de Water 2002) and DNS of forced stationary homogeneous turbulence (see data compilations by Sreenivasan 1998; Burattini *et al.* 2005). However, the fundamental difference with the present FSG-generated turbulence is that the C_ε asymptote for high Re_0 is different for different streamwise downstream locations. This is high Reynolds number non-Richardson–Kolmogorov behaviour

The key departure behind the present FSG-generated turbulence behaviour lies in the difference between the streamwise dependencies of L_u/λ and Re_λ ($A(x) \neq$

$B(x)$, see (1.4) and (1.5)). For steady initial conditions (fixed Re_0) there is a significant Re_λ decrease during decay (figure 7*b*), whereas L_u/λ stays approximately constant (figure 8*a*), leading to a steep monotonic downstream increase in the normalized dissipation rate C_ε (figure 7*a*) which follows approximately the form $C_\varepsilon \propto (L_u/\lambda)/Re_\lambda \sim Re_\lambda^{-1}$ (figure 8*b*). Note, in particular, how the C_ε versus Re_λ curve shifts to the right as Re_0 increases, which is clear evidence of the two independent dependencies that C_ε has on Re_λ and Re_0 in this fractal-generated turbulence.

Data were taken with probes of different spatial resolutions to confirm that these results are not meaningfully biased by the resolution of the measurements yielding figure 8 (see § 2.1 for details). Nonetheless it can be seen that the lesser resolution probe ($d_w \approx 5$ μm, $l_w \approx 1$ mm) has a slightly lower L_u/λ ratio due to the underestimation of $\overline{(\partial u/\partial x)^2}$, but it does not change the main observation that L_u/λ is effectively roughly constant, at least compared with the wide variation of Re_λ, during decay.

We now contrast the behaviour of our FSG-generated turbulence behaviour with that of the RG-generated turbulence. Such turbulence is thought to follow Richardson–Kolmogorov phenomenology, although it is usually difficult to exceed Reynolds numbers beyond $Re_\lambda \approx 150$ in typically sized laboratory wind tunnels (at least if Corrsin's restriction $x/M > 30$ is applied; Corrsin 1963) and therefore the RG experiments are commonly at the lower end of the range of validity of the Richardson–Kolmogorov phenomenology. Nevertheless, our RG data for $U_\infty = 20$ m s^{-1} appear to have sufficiently high Reynolds numbers to support $C_\varepsilon \approx constant$ (figure 8*b*) and related $L_u/\lambda \propto Re_\lambda$ (figure 8*a*). Furthermore it can be seen that the Re_λ dependence of C_ε falls on the same curve regardless of how Re_λ is varied, whether by varying Re_0 or by varying the streamwise position of the measurement. The same observation can be made for the curve L_u/λ versus Re_λ. This is well-defined Richardson–Kolmogorov behaviour where $A(x) = B(x)$, $\alpha = \beta = 1/2$ and consequently no distinction between local and global Reynolds number exists. Below $Re_\lambda \approx 120$, direct dissipation becomes noticeable and causes a departure from $C_\varepsilon \approx constant$, presumably due to an insufficiently large separation between outer and inner scales (Dimotakis 2000).

Summarizing, the present FSG-generated decaying turbulence is fundamentally and qualitatively different from RG-generated decaying turbulence. The $C_\varepsilon \approx constant$ behaviour is not observed in figure 8 for the FSG despite the moderately large turbulent Reynolds numbers Re_λ (around three times the Re_λ necessary for the RG to exhibit $C_\varepsilon = constant$ on this plot) and the evidence that the global/inlet Reynolds number Re_0 is sufficiently large for C_ε to be independent of Re_0 (figure 6). In fact, the normalized dissipation rate is closer to $C_\varepsilon \sim Re_\lambda^{-1}$ and $L_u/\lambda \approx constant$, which is in line with the previous experiments by Mazellier & Vassilicos (2010), although the larger length of the present wind tunnel brings evidence that L_u/λ and $C_\varepsilon Re_\lambda$ are not exactly constant in this tunnel, but are only roughly so for the entire decay region assessed. This might be an effect brought about, perhaps paradoxically, by the eventual low (although not too low) values of Re_λ far downstream. Or it might be due to a decrease in the growth of L_u because of the boundary layers at the tunnel walls which begin to have a significant thickness very far downstream in this longer wind tunnel. As this wall effect might not affect the growth of λ, L_u/λ would monotonically decrease downstream. Nevertheless, as we show later in this paper, the downstream evolutions of L_u/λ and C_ε are consistent with a self-preserving evolution of energy spectra which can be made to collapse with a single scale

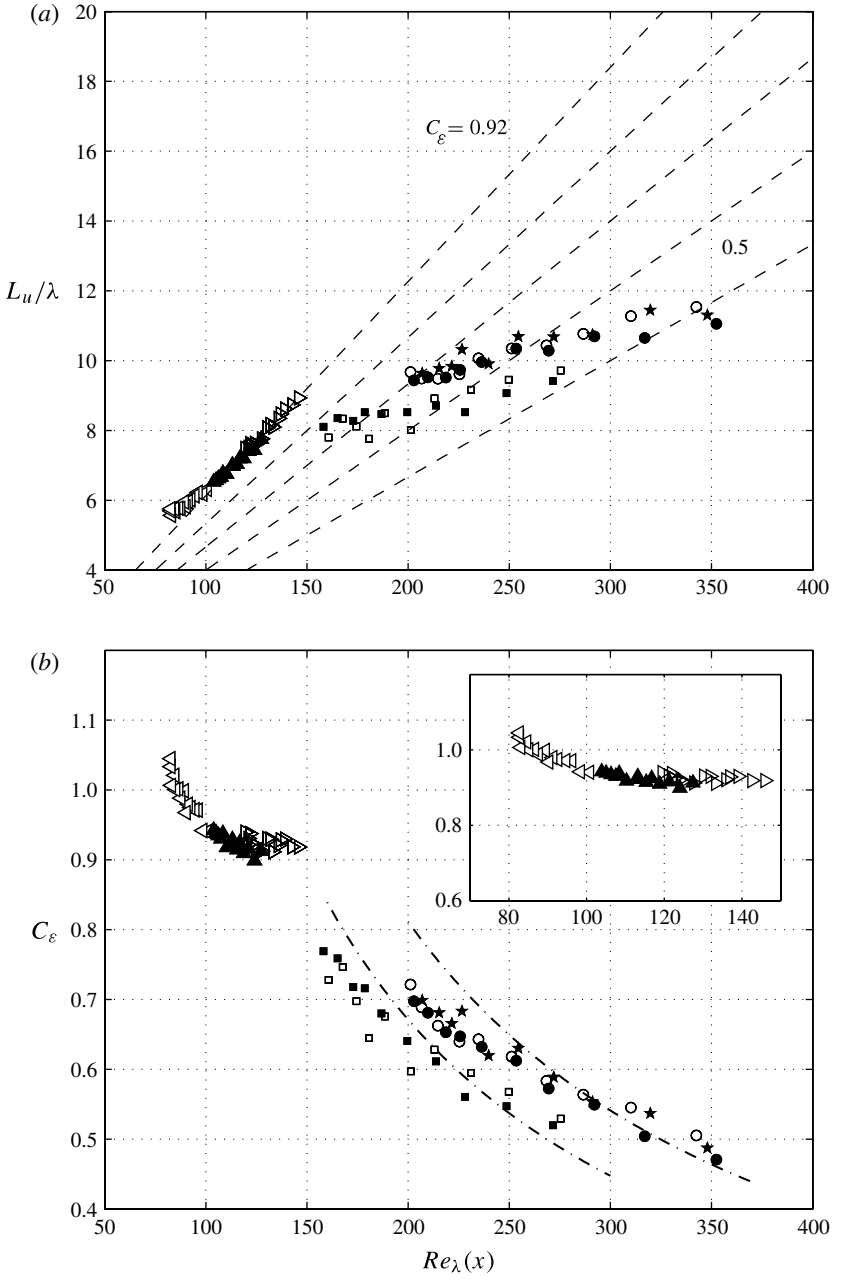

FIGURE 8. Local Reynolds number dependence $Re_\lambda(x)$ of (*a*) Integral length scale to Taylor microscale ratio L_u/λ and (*b*) normalized energy dissipation rate C_ε, for both the FSG and RG data recorded at different inlet velocities with a SW: (■) FSG recorded at $U_\infty = 10\ \mathrm{m\ s^{-1}}$ with a $l_w = 1$ mm sensing length SW, (□) FSG at $U_\infty = 10\ \mathrm{m\ s^{-1}}$, $l_w = 0.45$ mm, (●) FSG at $U_\infty = 15\ \mathrm{m\ s^{-1}}$, $l_w = 1$ mm, (○) FSG at $U_\infty = 15\ \mathrm{m\ s^{-1}}$, $l_w = 0.45$ mm, (⋆) FSG at $U_\infty = 15\ \mathrm{m\ s^{-1}}$, $l_w = 0.2$ mm, (◁) RG at $U_\infty = 10\ \mathrm{m\ s^{-1}}$, $l_w = 0.45$ mm, (▲) RG at $U_\infty = 15\ \mathrm{m\ s^{-1}}$, $l_w = 0.45$ mm, (▷) RG at $U_\infty = 20\ \mathrm{m\ s^{-1}}$, $l_w = 0.45$ mm. The dashed-dot lines follow the form $\propto Re_\lambda^{-1}$. The inset of the second figure is a zoomed plot of the RG data.

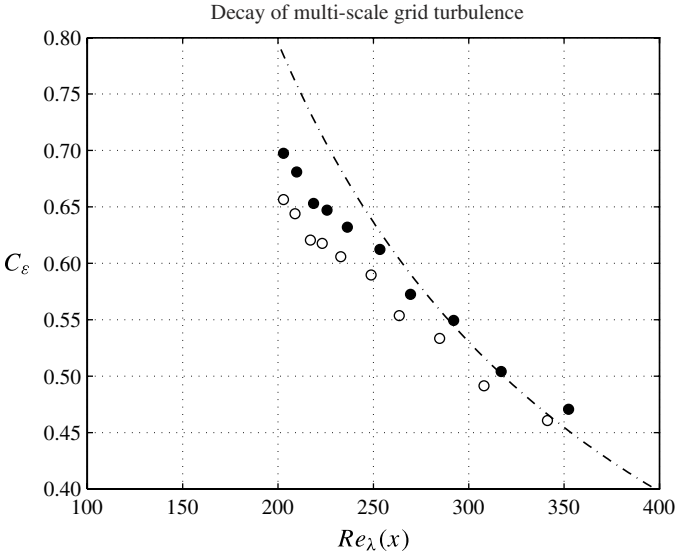

FIGURE 9. Uncertainty and bias due to large- and small-scale (an)isotropy in the observed normalized energy dissipation rate C_ε behaviour. In this specific plot we redefine u'^2 and ε to be $u'^2 \equiv \overline{u^2}(1 + 2\overline{v^2}/\overline{u^2})$, $\varepsilon \equiv \nu\,\overline{(\mathrm{d}u/\mathrm{d}x)^2}[3 + 6\overline{(\mathrm{d}v/\mathrm{d}x)^2}/\overline{(\mathrm{d}u/\mathrm{d}x)^2}]$ and take (•) the isotropic estimates $\overline{v^2}/\overline{u^2} = 1$ and $\overline{(\mathrm{d}v/\mathrm{d}x)^2}/\overline{(\mathrm{d}u/\mathrm{d}x)^2} = 2$ and (○) the anisotropy estimates of $\overline{v^2}/\overline{u^2}$ and $\overline{(\mathrm{d}v/\mathrm{d}x)^2}/\overline{(\mathrm{d}u/\mathrm{d}x)^2}$ from table 4. The dashed-dot line follows $\propto Re_\lambda^{-1}$.

reasonably well, as opposed to the two different inner and outer scales required by Richardson–Kolmogorov phenomenology.

Finally note that the large- and small-scale anisotropy (characterized by the ratios $u'/v' \approx 1.1$ and $\overline{(\mathrm{d}v/\mathrm{d}x)^2}/\overline{(\mathrm{d}u/\mathrm{d}x)^2} \approx 1.5$, see § 3.2.2 and table 4) change the exact numerical values of C_ε and Re_λ for each measurement location (see figure 9) and can be considered a source of uncertainty. Nevertheless, the main difference is an offset of the C_ε versus Re_λ curve and there is no meaningful change of its functional form.

3.4. *Energy decay*

The functional form of the turbulent kinetic energy decay is usually assumed to follow a power law, which is mostly in agreement with the large database of laboratory and numerical experiments for both grid-generated turbulence and boundary-free turbulent flows

$$\overline{u^2} \sim (x - x_0)^{-n} \tag{3.5}$$

where $\overline{u^2} \equiv u'^2$.

Mazellier & Vassilicos (2010) proposed a convenient alternative functional form for the kinetic energy decay (and for the evolution of λ when $U_\infty(\mathrm{d}/\mathrm{d}x)\overline{u^2} \propto \nu\overline{u^2}/\lambda^2$ is a good approximation) that is both consistent with the power-law decay and the exponential decay law proposed by George & Wang (2009):

$$\begin{cases} \lambda^2 = \lambda_0^2\left[1 + \dfrac{4\nu a|c|}{l^2(x_0)U_\infty}(x - x_0')\right] \\ \overline{u^2} = \dfrac{2\,u_0'^2}{3}\left[1 + \dfrac{4\nu a|c|}{l^2(x_0)U_\infty}(x - x_0')\right]^{(1-c)/2c} \end{cases} \tag{3.6}$$

where $c < 0$. In the limit of $c \to 0$ it asymptotes to an exponential decay with constant length scales throughout the decay, but otherwise it is a power-law decay where x_0 is not the conventional virtual origin where the kinetic energy is singular. The two equations (3.5) and (3.6) are equivalent with $n = (c-1)/2c$ and $x_0 = x_0' - l_0^2\, U_\infty/(4\nu ac)$.

Determining the decay exponent directly from (3.5) is difficult, although feasible, since a nonlinear fit is generally needed to determine n and x_0' simultaneously. For homogeneous (isotropic) turbulent decaying flow where advection balances dissipation it is possible to obtain a linear equation for the Taylor microscale that can be used to determine the virtual origin, thus simplifying the task of determining the decay exponent. Using $\lambda^2 = 15\nu\overline{u^2}/\varepsilon$ in conjunction with the advection dissipation balance characteristic of homogeneous isotropic turbulence ($3/2\, U\partial\overline{u^2}/\partial x = -\varepsilon$) and assuming power-law energy decay (3.5) we obtain

$$\lambda^2 = \frac{10\nu}{nU}(x - x_0). \tag{3.7}$$

Note that for λ^2 to be linear the mean velocity has to be constant otherwise the linear relation holds for $U\lambda^2$. Even though advection does not balance dissipation in our fractal-grid-generated decaying turbulence because of the significant presence of transverse energy transport as shown in § 3.2.1, transverse energy transport and dissipation remain approximately proportional to each other throughout the assessed decay region and for the range of values of U_∞ tried here. This suggests that

$$U\,\frac{\mathrm{d}}{\mathrm{d}x}\overline{u^2} \propto \nu\overline{u^2}/\lambda^2 \tag{3.8}$$

might be a good approximation for the decay region of our fractal-generated turbulence as is indeed supported by our data which show that $U\lambda^2$ grows linearly with downstream location and even that $U\lambda^2$ versus x collapses the data well for different inlet velocities U_∞ (see figure 10*a*).

The decay exponents of (3.5) and (3.6) are estimated using four alternative methods:

(i) Method I: linear fit to $U\lambda^2$ (3.7) to determine the virtual origin followed by a linear fit to the logarithm of (3.5) to determine the exponent n, as done by Hurst & Vassilicos (2007). Antonia *et al.* (2003) determined the virtual origin in a similar fashion by plotting $\lambda^2/(x - x_0)$ for different x_0 and choosing the virtual origin yielding the broadest plateau (which for their RG experiment was $x_0 \approx 0$).

(ii) Method II: the linearized logarithm method proposed in Mazellier & Vassilicos (2010) to determine the unknowns in (3.6).

(iii) Method III: direct application of a nonlinear least-squares regression algorithm ('NLINFIT' routine in MATLAB^{TM}) to determine the decay exponent and virtual origin simultaneously. This is related to the method used by Lavoie, Djenidi & Antonia (2007), but allowing the virtual origin to be determined by the algorithm as well. This method can be applied to (3.5) as well as to (3.6). Note that if applied to (3.5) as we do here, this fitting method does not necessarily yield a virtual origin compatible with (3.7).

(iv) Method IV: assume that the virtual origin coincides with the grid location and linearly fit the logarithm of (3.5). This crude method typically yields biased estimates of the decay exponent, since there is no *a priori* reason for the virtual origin to be zero. Nevertheless this is a robust method typically used to obtain

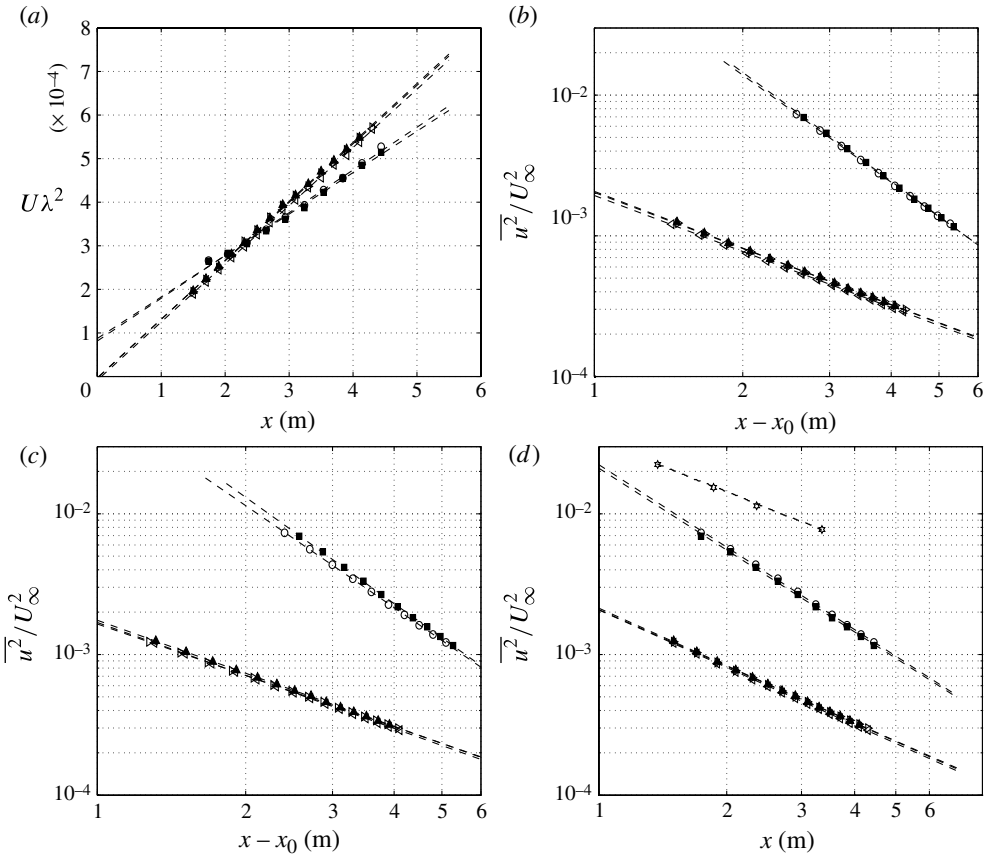

FIGURE 10. Decay of turbulence generated by the RG and the FSG: (*a*) linear growth of $U\lambda^2$, (*b*) power-law fit using method I, (*c*) power-law fit using method III and (*d*) power-law fit using method IV. (■) FSG at $U_\infty = 10\ \mathrm{m\ s^{-1}}$, (○) FSG at $U_\infty = 15\ \mathrm{m\ s^{-1}}$, (◁) RG at $U_\infty = 10\ \mathrm{m\ s^{-1}}$, (▲) RG at $U_\infty = 15\ \mathrm{m\ s^{-1}}$, (▷) RG at $U_\infty = 20\ \mathrm{m\ s^{-1}}$, (⋆) data from the active-grid experiment by Mydlarski & Warhaft (1996).

Grid	U (m s^{-1})	Method I		Method II	Method III		Method IV
		n	x_0/x_*	$(1+c)/2c$	n	x_0/x_*	n
RG	10	1.32	0.18	4.34	1.25	0.53	1.36
RG	15	1.34	0.08	5.04	1.25	0.52	1.36
RG	20	1.32	0.06	5.47	1.21	0.63	1.33
FSG	10	2.57	−0.31	7.10	2.51	−0.28	1.93
FSG	15	2.53	−0.28	8.01	2.41	−0.22	1.95

TABLE 5. Decay exponents and virtual origin estimation using different methods.

first-order estimates of power-law decay exponents in many flows (e.g. the active-grid data by Mydlarski & Warhaft 1996).

A main difference between these methods is the way of determining the virtual origin, which has an important influence on the decay exponent extracted. This

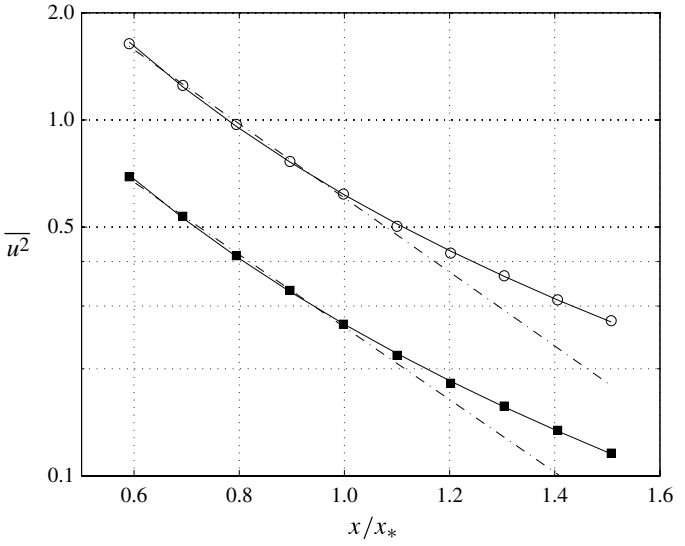

FIGURE 11. Turbulent kinetic energy decay of turbulence generated by the FSG fitted to (3.6) using method II (dashed-dot line) and method III (solid line). The data range used in method II is $0.6 < x/x_* < 1.1$, which corresponds to the streamwise region assessed by Mazellier & Vassilicos (2010). Streamwise data was taken at two fixed inlet velocities: (■) $U_\infty = 10\ \mathrm{m\ s^{-1}}$, (○) $U_\infty = 15\ \mathrm{m\ s^{-1}}$. Note that for $0.6 < x/x_* < 1.1$ the two methods appear to fit the data reasonably well, but further downstream the differences become evident.

inherent difficulty in accurately determining the decay exponent is widely recognized in the literature (see e.g. Mohamed & LaRue 1990).

The decay data for the RG- and FSG-generated turbulence are well approximated by the curve fits obtained from methods I and III (see figure 10*b* and *c*) and the numerical values of the exponents change only marginally (see table 5). On the other hand method IV also seems to fit the data reasonably well (see figure 10*d*), but the exponents retrieved for the fractal-grid data are $n \approx 2$, slightly lower than the exponents predicted by the other methods $n \approx 2.5$. The virtual origin which is forced to $x_0 = 0$ in method IV leads to a slight curvature in the $\log(\overline{u^2})$ versus $\log(x)$ data (almost imperceptible to the eye, compare the fractal-grid data in figure 10*c* and *d*) and a non-negligible bias in the estimated exponents. Nevertheless the difference in the power laws describing the measured RG- and FSG-generated turbulence is quite clear. For completeness, the results from the experimental investigation by Mydlarski & Warhaft (1996) on decaying active-grid-generated turbulence are added in figure 10*d*. They applied a fitting method equivalent to method IV and reported a power-law fit yielding a decay exponent $n = 1.21$. Kang *et al.* (2003) employed the same method to their active-grid-generated turbulence data and retrieved a similar result, $n = 1.25$.

Note that there are residual longitudinal mean velocity gradients (which cause a residual turbulence production of about 3 % of the dissipation, see § 3.2.1) and therefore it is preferred to fit $\overline{u^2}$ data rather than $\overline{u^2}/U^2$ data. Nevertheless we checked that fitting $\overline{u^2}/U^2$ data does not meaningfully change the results nor the conclusions.

Concerning method II it can be seen (table 5) to be the most discrepant of the four methods yielding a much larger decay exponent. This method was proposed by Mazellier & Vassilicos (2010) to fit the general decay law (3.6) and is based on the

linearization of the logarithm appearing in the logarithmic form of (3.6), i.e.

$$\log(u'^2) = \log\left(\frac{2\,u_0'^2}{3}\right) + \left[-\frac{1+c}{2c}\right]\log\left(1+\frac{4\nu ac}{\lambda_0^2 U_\infty}(x-x_0')\right). \tag{3.9}$$

Linearization of the second logarithm on the right-hand side of (3.9) assumes $(4\nu ac/\lambda_0^2 U_\infty)(x-x_0') \ll 1$. This quantity, as we have confirmed in our data, is indeed smaller than unity and for the farthest position $4\nu ac/(l^2(x_0)U_\infty)(x-x_0) \approx 0.3$, but the fact that this linearized method does not yield results comparable to methods I and III suggests that the linearization of the logarithm may be an oversimplification. In figure 11 the kinetic energy decay data of turbulence generated by the FSG is shown along with the fitted curves obtained from methods II and III in a plot with a logarithmic ordinate and a linear abscissa. If in figure 11 the data taken at positions beyond $x/x_* = 1.05$ are excluded we can compare the present results with those presented in Mazellier & Vassilicos (2010) where the data range was limited to $0.5 < x/x_* < 1.05$. Visually, for that data range, the two different fitting methods appear to fit the data reasonably well and thus the linearization of the logarithm in (3.9) is justified in this limited range. Note, however, that the two fitting methods yield very different decay exponents because they also effectively yield different virtual origins: for example at $U_\infty = 15$ m s^{-1} method III yields $(1+c)/(2c) \approx -2.4$ whereas method II yields $(1+c)/(2c) \approx -8.0$. If no data is excluded from figure 11, it can clearly be seen that the two methods produce very different curves and very different decay exponents (note, however, that the use of a longer test section, which allows the assessment of the decay behaviour further downstream, comes at the cost of having thicker boundary layers developing at the walls which can have an increasing influence on the largest turbulent eddies, as discussed in § 3.2.3).

3.4.1. *Influence of transverse transport on power-law decay exponent*

It is shown in § 3.2.1 that dissipation does not balance the advection but that the two are roughly proportional throughout the measured decay region of the FSG-generated turbulence. It is also shown in that section that this imbalance is mostly due to transverse triple-correlation transport which remains roughly 50–60 % of the dissipation throughout the measured region (with no clear increasing or decreasing trend), whereas turbulence production and longitudinal triple-correlation transport terms become negligible well before $x < x_*$. Pressure transport, calculated from the kinetic energy balance, may also play a noticeable role of countering a fraction (typically between 1/4 and 1/3) of the triple-correlation transport. Based on these results, (3.3) which holds at the centreline reduces to

$$\frac{U}{2}\frac{\partial\overline{q^2}}{\partial x} = -\varepsilon + \left[-2\frac{\partial}{\partial y}\frac{\overline{vq^2}}{2} + \Pi\right]. \tag{3.10}$$

The decay rate of the kinetic energy as the turbulence is advected downstream (effectively the advection term) is now determined both by viscous dissipation and by a net effect of removing energy from the centreline and transporting it to the sides. As in the portion of the decay region of the fractal-generated turbulence where we take measurements this loss rate to the sides remains approximately proportional to the dissipation rate, i.e.

$$\frac{U}{2}\frac{\partial\overline{q^2}}{\partial x} = -\chi\,\varepsilon \tag{3.11}$$

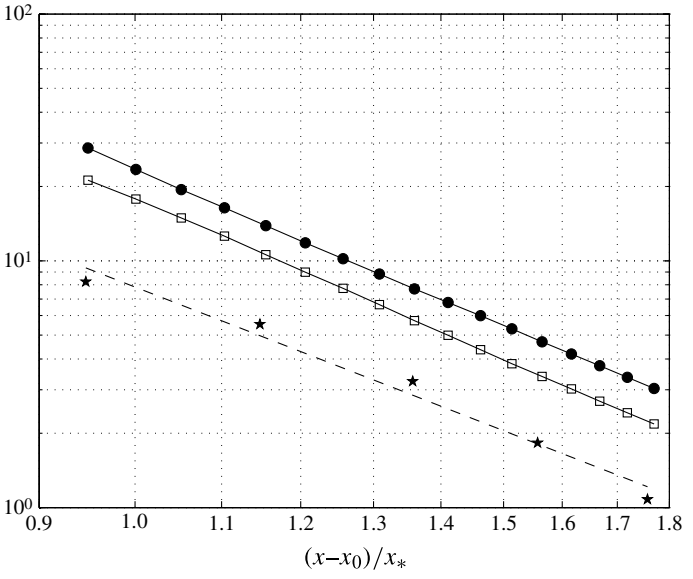

FIGURE 12. Downstream decay of: (●) kinetic energy $\frac{U}{2}\frac{\partial\overline{q^2}}{\partial x}$, (□) dissipation ε, (⋆) transverse triple-correlation transport $2(\partial/\partial y)(\overline{vq^2}/2)$, for $U = 15$ m s^{-1}.

where $\chi = 1+[\partial\overline{vq^2}\partial y-\Pi]/\varepsilon \approx 1.5$ (figure 2*c*), we can expect the decay exponent n to be set by the dissipation rate ε (irrespective of what sets the dissipation rate). Indeed, the higher power-law decay exponents exhibited by the fractal-generated turbulence can be accounted for by the fact that $C_\varepsilon \sim Re_\lambda^{-1}$ (see § 3.3) and consequently the steep increase of $C_\varepsilon = \varepsilon L_u/u'^3$ with streamwise location. In other words, an increasing proportion of u'^3/L_u is being dissipated at increasing streamwise locations which leads to an increase in the power-law decay exponent relative to the $C_\varepsilon = constant$ case.

In figure 12 we plot on a logarithmic scale the streamwise decay of the advection, the dissipation and the transverse triple-correlation transport (which are all measured independently) and they indeed seem to follow straight lines (i.e. power laws) with the same slope (i.e. power-law exponent), thus supporting our argument.

To further substantiate our argumentation one more set of experiments were conducted. Anemometry measurements at an inlet velocity of $U_\infty = 15$ m s^{-1} using a $l_w = 0.5$ mm sensing length SW were recorded between $0.63 < x/x_* < 1.44$ along four parallel lines aligned with the mean flow and crossing the grid at $z = 0, 0, 20, 20$ mm and $y = 0, 40, 80, 120$ mm ($z = 0$ is the vertical plane of symmetry of the grid). From the transverse triple-correlation transport measurements for $z = 0$ (figure 3*b*) we expect the contribution from this term to be very different at the centreline (where it is maximal) and off the centreline where it can be roughly zero ($y \approx 80$) or negative ($y > 100$). However, if a value of χ can be defined that is constant throughout the streamwise decay range assessed here for each transverse (y, z) position, then the argument outlined in the previous two paragraphs will hold even if χ varies with transverse positions, as indeed it does. The consequence is that, in the decay region assessed, the decay exponent n should remain about the same at all of these transverse positions and also remain unusually large due to the C_ε behaviour. The data for the different transverse locations are fitted using method III and the results (see table 6) are encouraging. In spite of some variation in the best fit power-law decay exponents,

y (mm)	n	$x_0/x_\star$
0	2.42	−0.27
40	2.61	−0.29
80	2.27	−0.11
120	2.63	−0.39

TABLE 6. Decay law estimates along four parallel streamwise oriented lines at the centreline and off the centreline between $0.63 < x/x_\star < 1.40$ obtained from method III.

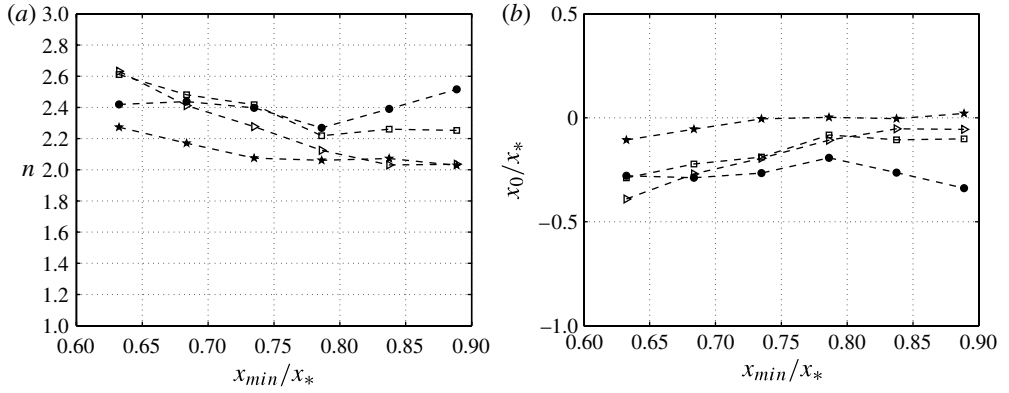

FIGURE 13. Decay law estimates for different data ranges $x_{min} < x/x_\star < 1.40$, $U = 15$ m s^{-1}: (●) $y = 0$ mm, (□) $y = 40$ mm, (⋆) $y = 80$ mm, (▷) $y = 120$ mm. (*a*) Decay exponent n and (*b*) virtual origin $x_0/x_\star$ obtained from method III.

the numerical values of these exponents are all relatively close to each other ranging between 2.3 and 2.6. We note that these exponents are larger than all boundary-free turbulent flows listed in table 1.

Finally, as some presence of turbulence production and longitudinal transport remains for some distance downstream of $x_{peak} \approx 0.45x_*$ (although not in any significant way beyond x_*) we explore how the power-law fits of the turbulence energy decay change when the smallest streamwise location considered in the fit is increased. We do this both for centreline and off-centreline data and report our results in figure 13. On the centreline the decay exponent and virtual origin remain approximately the same within the scatter ($n \approx 2.4, x_0/x_* \approx -0.3$), but they show a respectively decreasing/increasing tendency off-centreline up to $x/x_* \approx 0.8$. At any rate, the decay exponents $n > 2.0$ for all our data.

In conclusion the decay exponents for the present fractal-generated turbulence measured both at the centreline and off the centreline in the region $0.6 < x/x_* < 1.5$ are consistently higher than those in all boundary-free turbulent flows listed in table 1 and much higher (by a factor between 4/3 and 2) than those of decaying turbulence generated by RGs and active grids (Mydlarski & Warhaft 1996; Kang *et al.* 2003). It might be interesting to note that in many boundary-free turbulent flows a conserved quantity such as $u'^2L^{M+1} = constant$ exists. Look at table 1 and note that $M = 1, 3, 5, 7$ for the four wakes, $M = -1$ for the mixing layer, $M = 0, 1$ for the jets and $M \geqslant 2$ for RG turbulence. If the flow is also such that $U\,\mathrm{d}u'^2/\mathrm{d}x \propto -\varepsilon$, then $C_\varepsilon = constant$

implies

$$n = \frac{2(M+1)}{M+3} \tag{3.12}$$

and $C_\varepsilon \sim Re_\lambda^{-1}$ implies

$$n = \frac{M+1}{2} \tag{3.13}$$

(which is larger than $n = 2(M+1)/(M+3)$ provided that $M > 1$). Considering, for example, the range $M \geqslant 2$, the exponent n corresponding to $C_\varepsilon \sim Re_\lambda^{-1}$ is at least $5/4$ times larger than the exponent n corresponding to $C_\varepsilon = constant$, and is generally much larger. If $M = 3$ or $M = 4$, then $C_\varepsilon \sim Re_\lambda^{-1}$ implies $n = 2$ or $n = 2.5$, close to what is observed here, whereas $C_\varepsilon \sim constant$ implies $n = 4/3$ or $n = 10/7$.

At this stage we do not have any proof that a conserved quantity such as $u'^2 L^{M+1} = constant$ exists for our fractal-generated turbulence. The previous paragraph is therefore only indicative and serves to illustrate how a C_ε which is a decreasing function of Re_λ can cause the decay exponent to be significantly larger than a C_ε which is constant during decay and can even return decay exponents comparable to those observed here. Of course the decaying turbulence we study in this work is not perfectly homogeneous and isotropic because of the presence of transverse turbulent transport of turbulent kinetic energy and therefore significant gradients of third-order one-point velocity correlations. As a consequence, a conserved quantity such as $u'^2 L^{M+1} = constant$, if it exists, cannot result from a two-point equation such as the von-Kármán–Howarth equation for homogeneous turbulence (see Vassilicos 2011). We leave the investigation of conserved quantities in third-order inhomogeneous decaying turbulence such as the present one for the future (we include gradients of pressure–velocity correlations in the term 'third-order inhomogeneous').

Nevertheless, it is clear that the dissipation rate of kinetic energy is increasingly larger than u'^3/L as the turbulence moves further downstream in cases such as the present one where C_ε increases in approximate proportion to $1/Re_\lambda$ as the turbulence and Re_λ decay. In the absence of any other type of loss or gain of kinetic energy, and assuming no counter effect of C_ε on the integral scale, a much steeper decay (e.g. much larger exponent n) will result than if C_ε was constant during decay. In the present case where loss of energy also occurs by turbulent transport, see (3.10), this conclusion can remain the same in the region assessed only if, in that region, the loss of energy by turbulent transport remains proportional to the loss of energy by dissipation, as indeed observed.

The question then naturally arises whether this balance between turbulent transport and dissipation persists for the entire decay range all the way to very large values of x/x_*, much larger than those accessible here. If it does, then the implication is that perfectly homogeneous isotropic turbulence is impossible at any stage of the decay. If it does not and if turbulent transport starts to decay much faster than dissipation beyond a certain x/x_*, then a turbulence that is third-order homogeneous and isotropic may well appear if it has the time to do so before the final stages of decay. If C_ε continues to increase nearly as $1/Re_\lambda$ in such a third-order homogeneous isotropic turbulence then the decay will remain exceptionally fast with values of n such as the present values. However, it may be that the unusual behaviour observed here for the dissipation rate ε (a two-point statistic) is in fact the result of gradients in particular one-point statistics such as third-order velocity correlations and pressure–velocity

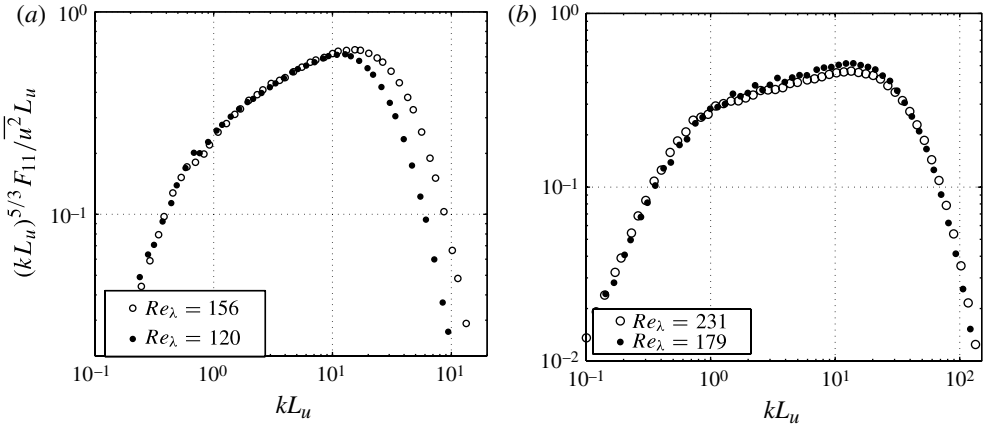

FIGURE 14. Compensated one-dimensional energy spectra, normalized with $\overline{u^2}, L_u$ at two streamwise locations for the (*a*) RG-generated and (*b*) FSG-generated turbulence data. Both plots have roughly the same Reynolds number ratio, $Re_{\lambda_1}/Re_{\lambda_2} \approx 1.3$ (see Appendix). The data are recorded at $U_\infty = 20$ m s^{-1} and $U_\infty = 10$ m s^{-1} respectively.

correlations, i.e. inhomogeneities. Either way, the consequences can be far reaching and call for much future research, in particular re-examinations of Reynolds number dependencies of C_ε in all manner of turbulent flows, in particular boundary-free turbulent flows such as those listed in table 1.

As a final remark, note that the data points for transverse turbulent transport in figure 12 seem to curve downwards at high x/x_*. However, we cannot extrapolate much from this observation as we do not measure pressure directly and we do not know how gradients of pressure–velocity correlations curve at high x/x_*.

3.5. *Collapse of the energy spectra and structure functions*

As explained in Seoud & Vassilicos (2007) and Mazellier & Vassilicos (2010) single-length scale self-preserving energy spectra can allow for $L_u/\lambda = constant$ during decay. This can be assessed by plotting the normalized energy spectra for different positions along the mean flow direction and evaluating the collapse of the data or the lack thereof. It should be mentioned that the three-dimensional energy spectrum and one-dimensional energy spectra can be shown to be equivalent for an isotropic flow. It should also be noted that the flow is not exactly isotropic as discussed in § 3.2.2, so we might expect some effect on the spectral collapse.

3.5.1. *One-dimensional energy spectra*

We begin by illustrating the qualitative difference between the collapse of the normalized energy spectra (using large scale variables: u'^2, L_u) of turbulence generated by the RG and by the FSG, see figure 14. The data for the RG are taken in a region where $L_u/\lambda \propto Re_\lambda$ and $C_\varepsilon \approx constant$, see figure 8. The normalized spectra measured in the lee of the RG show a good collapse at the low frequencies but not at the high frequencies, which is in line with Kolmogorov's theory. On the other hand it can be seen that the normalized turbulence spectra generated by the FSG appears to collapse at all frequencies, in line with the single-length-scale assumption as previously observed by Mazellier & Vassilicos (2010).

In order to complement the previous results, the assessed decay region is extended allowing to further test the single-length-scale assumption. The normalized spectra

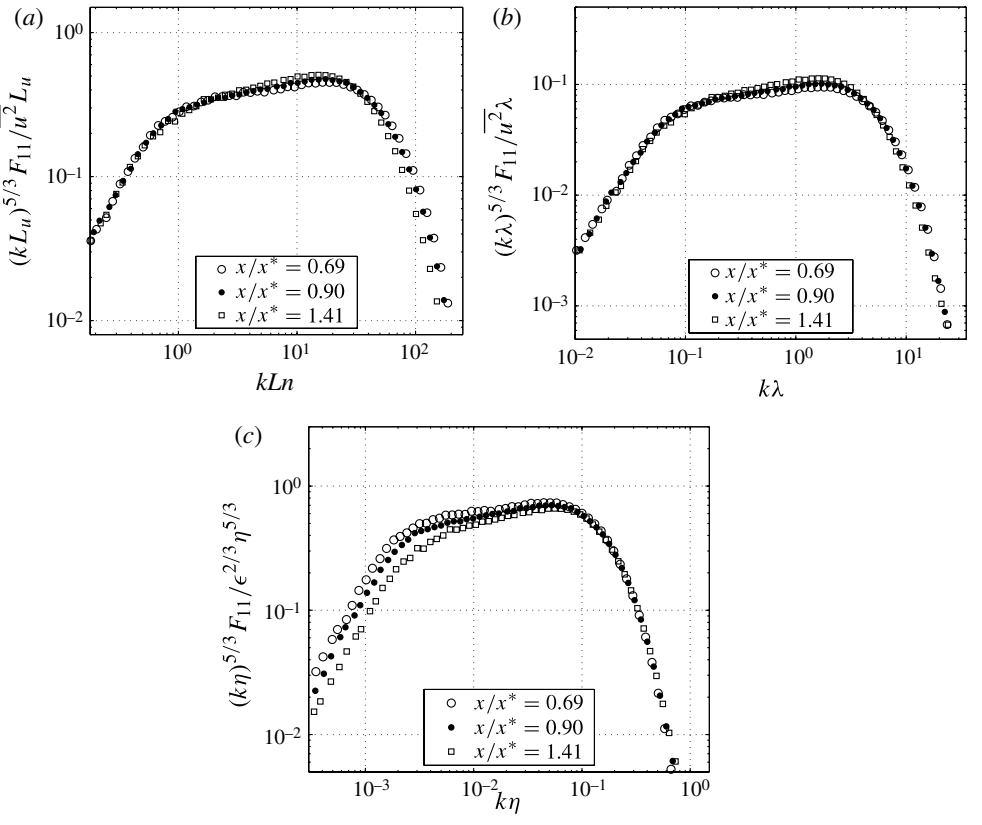

FIGURE 15. Compensated one-dimensional energy spectra of turbulence generated by the FSG at three streamwise downstream locations ($Re_\lambda = 324, 273, 210$) at $U_\infty = 15\ \mathrm{m\ s^{-1}}$, normalized by (*a*) $\overline{u^2}$ and L_u, (*b*) $\overline{u^2}$ and λ and (*c*) ν and ε.

of decaying turbulence downstream of our FSG are shown in figure 15 using both the integral scale and the Taylor microscale. For the extended region it can be seen that the normalized spectra using the Taylor microscale do collapse for the entire frequency range, although the collapse using the integral scale at high frequencies is modest for $kL_u > 40$ where the furthermost point ($x/x_* = 1.41$) is taken into account. However, the discrepancy between data at $Re_\lambda = 324$ and $Re_\lambda = 210$ is much too small compared with the lack of collapse which would occur if the data obeyed Richardson–Kolmogorov scaling as in figure 14(*a*). It should be noted that in theory the collapses with L_u or with λ should be identical if $L_u \propto \lambda$, but as was seen in figure 8 this is not verified exactly in our wind tunnel's extended test section.

Nevertheless, in Appendix we propose a methodology for making a rough estimate of the quality of collapse of normalized spectra at high frequencies and we find that it depends on the logarithm of the Reynolds number ratio $Re_{\lambda_1}/Re_{\lambda_2}$ at two streamwise distances $x = \xi_1$ and $x = \xi_2$ with a prefactor which depends on the behaviour of L_u/λ during decay. In the Appendix, we apply this methodology to the active-grid data of Kang *et al.* (2003), for which there is evidence of a Richardson–Kolmogorov cascade, and show how spectral collapse with outer variables can be misleading because the Reynolds number ratio is small. The same methodology applied to our data shows

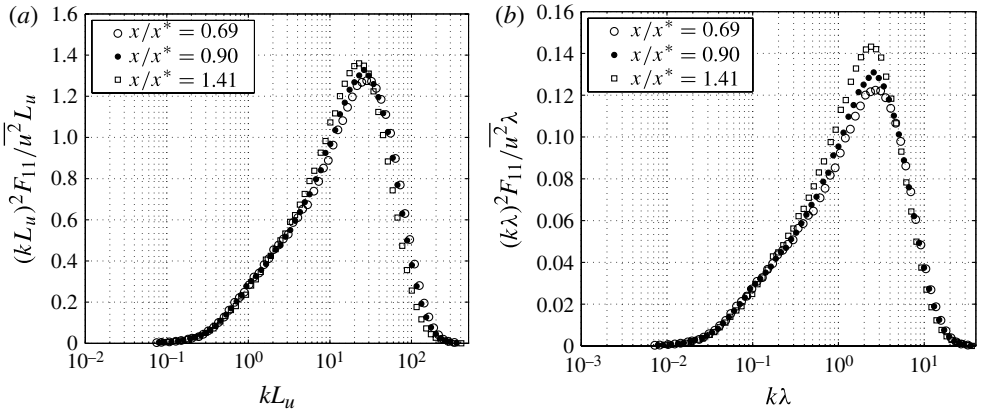

FIGURE 16. Compensated one-dimensional energy spectra of turbulence generated by the FSG at three streamwise downstream locations corresponding to $Re_\lambda = 324, 273, 210$ at $U_\infty = 15$ m s^{-1}, normalized by (*a*) $\overline{u^2}$ and L_u and (*b*) $\overline{u^2}$ and λ.

that we are not fully able to conclude on the very-high-frequency end of fractal-grid-generated energy spectra.

Premultiplying the one-dimensional energy spectra by the square of the frequency yields the Fourier spectrum of $\overline{(\mathrm{d}u/\mathrm{d}x)^2}$, so a second test to the single-length scale assumption is to assess the collapse of this isotropic equivalent of the dissipation spectra. The data, plotted in figure 16 show a reasonable collapse onto a single curve using both length scales, although it can be seen that the peak of the premultiplied spectra does not collapse perfectly. This may, to some extent, be an effect of the slight anisotropy of the flow, since it affects the large-scale variables the normalization is based on. It is shown in the following section how it is possible to partly account for this effect by computing the three-dimensional energy spectrum.

3.5.2. *Three-dimensional energy spectra*

The three-dimensional energy spectrum is computed using the two-component velocity signal from the XW measurements, with a similar algorithm to that presented in Helland & Van Atta (1977). The central assumption of the algorithm is isotropy in order to relate the one-dimensional total energy spectrum $F_{ii}(k_1) = F_{11}(k_1) + F_{22}(k_1) + F_{33}(k_1)$ with the three-dimensional spectrum $E(k)$,

$$E(k) = -k_1 \frac{dF_{ii}}{dk_1} \tag{3.14}$$

where the transverse one-dimensional spectra are considered to be approximately the same, i.e. $F_{22}(k_1) \approx F_{33}(k_1)$. The first derivative of the spectrum is computed using the logarithmic derivative proposed by Uberoi (1963):

$$E(k) = -F_{ii} \frac{\mathrm{d}\ln F_{ii}}{\mathrm{d}\ln k_1} \tag{3.15}$$

The three-dimensional energy spectrum was evaluated at 50 logarithmically spaced frequencies, and a second-order polynomial was fitted between two neighbouring frequencies using a least-squares fit in order to obtain a smooth derivative of the spectrum.

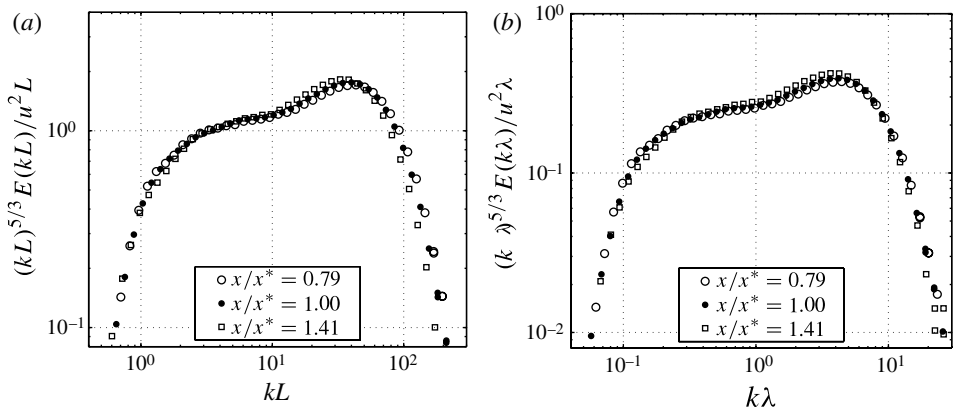

FIGURE 17. Three-dimensional energy spectra of turbulence generated by the FSG at three streamwise downstream locations corresponding to $Re_\lambda = 300, 238, 210$ at $U_\infty = 15\ \mathrm{m\ s^{-1}}$ and normalized by (*a*) $\overline{u^2} = 2/3\overline{q^2}$ and L and (*b*) $\overline{u^2}$ and λ.

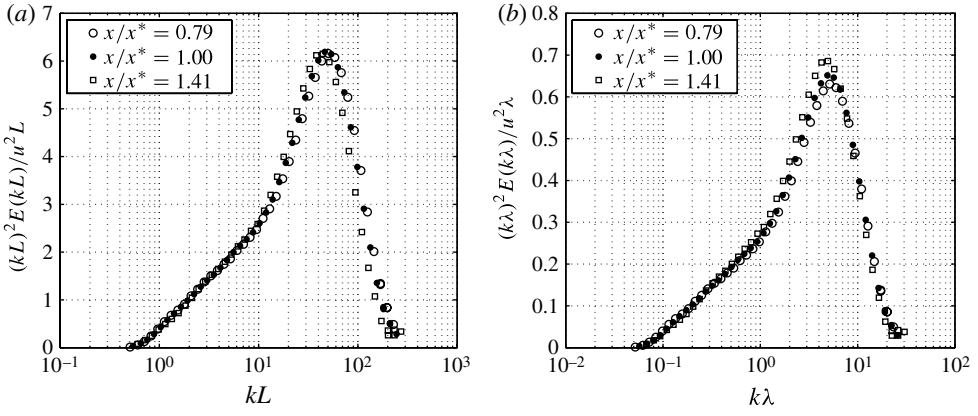

FIGURE 18. Enstrophy spectra of turbulence generated by the FSG at three streamwise downstream locations corresponding to $Re_\lambda = 300, 238, 210$ at $U_\infty = 15\ \mathrm{m\ s^{-1}}$ and normalized by (*a*) $\overline{u^2} = 2/3\overline{q^2}$ and L and (*b*) $\overline{u^2}$ and λ.

From the three-dimensional energy spectrum the integral scale L, the turbulent kinetic energy and the Taylor microscale can be recovered. The difficulty in accurately determining the low-frequency range of the energy spectra and consequently estimating the integral length scale should be noted. For this reason, the assessment of the spectrum's slope near $k \to 0$ was not possible.

The normalized compensated spectra are shown in figure 17, while the normalized enstrophy spectra are shown in figure 18. It is rewarding to see that the collapse of the three-dimensional energy spectrum presents less scatter than the one-dimensional spectrum thus offering support to the self-preserving single-length behaviour of turbulence generated by the FSG. Hence, some of the deviation from single-scale self-similarity collapse of the one-dimensional spectra in figures 15 and 16 is due to the moderate level of anisotropy present in the turbulence.

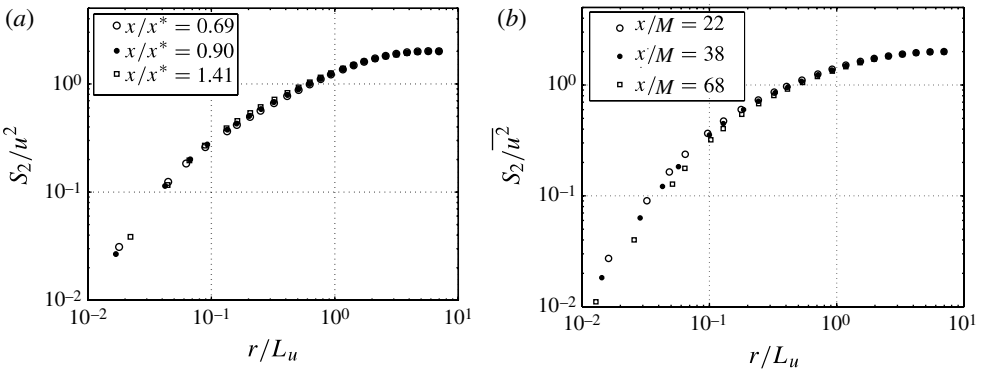

FIGURE 19. Second-order structure function at three streamwise downstream locations normalized by $\overline{u^2}$ and L_u: (*a*) FSG recorded at $U_\infty = 15\ \mathrm{m\ s^{-1}}$, $Re_\lambda = 323, 273, 210$ for $x/x_* = 0.69, 0.90, 1.41$; (*b*) RG recorded at $U_\infty = 20\ \mathrm{m\ s^{-1}}$, $Re_\lambda = 156, 137, 120$ for $x/M = 22, 38, 68$.

3.5.3. *Second-order structure functions*

The collapse of the second-order structure functions using u'^2 and L_u is shown in figure 19(*a*). Similarly to what has already been discussed for the spectra, this structure function collapses well at both low and high separations in the case of our fractal-generated turbulence. However, this is clearly not the case for the turbulence generated by the RG (see figure 19*b*).

4. Conclusions and issues raised

The decay of RG- and FSG-generated turbulence have been experimentally investigated using constant-temperature hot-wire anemometry. The main contribution of the present work is to complement previous research on the decay of fractal-grid-generated turbulence (e.g. Hurst & Vassilicos 2007; Seoud & Vassilicos 2007; Mazellier & Vassilicos 2010) by doubling the extent of the assessed decay region with the aim of investigating the persistence (or lack thereof) of the reported high decay exponents and the suppressed Richardson–Kolmogorov cascade. The present experimental investigation also complements the previous research by studying the effect of the hot-wire spatial resolution, carefully assessing the homogeneity of the flow during decay and taking anisotropy into account in the energy spectra.

We find that for streamwise downstream positions beyond $x/x_* \approx 0.6$ the turbulence is close to homogeneous except for a persistence of pressure transport and transverse energy transport and decays such that $L_u/\lambda \approx constant$ whilst Re_λ sharply decreases, at least up to the furthermost downstream position investigated. However, L_u/λ increases with increasing grid Reynolds number, e.g. $Re_0 = U_\infty t_0/\nu$. This observation is in direct conflict with the Richardson–Kolmogorov cascade (Mazellier & Vassilicos 2010), believed to be dominant at this range of Taylor-based Reynolds numbers Re_λ in various boundary-free turbulent flows, including RG- and active-grid-generated turbulence (Sreenivasan 1984, 1998; Burattini *et al.* 2005). It must be noted, however, that the vast majority of existing data is taken at fixed streamwise locations x and varying inlet Reynolds numbers Re_0 and as we show in § 3.3 for fractal-grid-generated turbulence, the streamwise downstream Reynolds number dependence $Re_\lambda(x)$ is not necessarily the same.

We observe that the energy spectra and the second-order structure function are much better described in the present FSG-generated turbulence by a single-scale self-similar form than by Kolmogorov (1941) phenomenology. Note that by Kolmogorov (1941) phenomenology we mean not only the necessity of two dynamically relevant sets of variables, outer and inner, that collapse the low- and the high-frequency part of the spectra respectively, but also that $L_u/\lambda \propto Re_\lambda$ and $C_\varepsilon = constant$, which implicitly dictates the rate of spreading of the high-frequency part of the spectra normalized by outer variables and vice versa. That turbulence generated by the present FSG does not obey Kolmogorov (1941) phenomenology is clear, for example, from the comparison between figure 14(*a*) and (*b*).

We also confirm the observations of Hurst & Vassilicos (2007) and Mazellier & Vassilicos (2010) concerning the abnormally high power-law decay exponents, compared with most boundary-free turbulent flows (see table 1), in particular RG- and active-grid-generated turbulence ($n_{FSG} \gg n_{RG}, n_{AG}$ by a factor between 4/3 and 2), and we confirm their persistence further downstream (at least up to $x/x_* \approx 1.5$). However, our results do not support the view in Hurst & Vassilicos (2007) and Mazellier & Vassilicos (2010) that the turbulence decay is exponential or near-exponential. We infer, by comparing our experimental results with the active-grid experiments of Mydlarski & Warhaft (1996), that the reason for the very unusual turbulence decay properties generated by the FSGs cannot be a confinement effect arising from the lateral walls. The two experimental investigations report completely different turbulence properties during decay, even though both experiments were performed on a similar sized wind tunnel and, in fact, the integral length scales generated by our FSG are typically less than half the integral length scales generated by the active grid. Our fractal-generated turbulence is third-order inhomogeneous in the sense discussed in § 3.4.1 but, to the best of the authors' knowledge, no homogeneity studies of active-grid-generated turbulence exist to date which are as thorough as that presented here, and it is therefore not possible to fully compare homogeneity and isotropy levels of the two types of turbulence. The presence/absence of turbulent transport of pressure and kinetic energy have not been investigated in sufficient detail in either active-grid- or RG-generated turbulence and it remains unknown to what degree and how far downstream these types of turbulence are third-order homogeneous and isotropic.

Although we find a general agreement with the previous results on the decay of fractal-grid-generated turbulence, some new issues are raised by the present experimental results due to the extended wind-tunnel test section. We find that L_u/λ is in fact not perfectly constant, but slowly decreases with Re_λ, and that the spectral collapse using large-scale variables is not perfect at very high wavenumbers as it ought to be for exact single-scale self-preserving turbulence decay. Possible causes for these two observations will be investigated in future work and include: (i) small-scale corrections to the single-scale self-preservation, (ii) moderately low Reynolds number limit to the validity of single-scale self-preservation and (iii) excessive thickness of the confining wall boundary layers far downstream interfering with the growth of the largest eddies of the turbulent flow due to insufficient ratio between the wind-tunnel width and the integral length scale.

As a final remark we note that the study of freely decaying turbulence requires experiments where (i) a wide range of Re_0 can be achieved by modifying the initial conditions and (ii) a wide range of Re_λ values must be straddled during decay. This

is emphasized by the analysis presented in Appendix where we give quantitative criteria for truthful spectral collapse and where we show, in particular, that whereas active grids generate high Reynolds numbers, they also generate a narrow logarithmic range of Reynolds numbers during decay thus making it impossible to confirm the Richardson–Kolmogorov cascade via spectral collapse.

So far, only modest ranges of Re_λ during decay have been achieved with RG- and active-grid-generated turbulence due to the typically slow decay rates of the turbulence they generate. The FSG-generated turbulence offers the unprecedented possibility of generating high-intensity decaying turbulence with a very wide range of Re_λ values during decay and approximately homogeneous mean flow and turbulence intensity profiles.

We are grateful to C. Meneveau, B. Lüthi and one anonymous referee for numerous suggestions which have helped us to very significantly improve the paper. P.C.V. acknowledges the support of the Portuguese Foundation for Science and Technology (FCT) under grant number SFRH/BD/61223/2009. The support from Dantec Dynamics Ltd (UK) in the design of the sine-wave testing hardware is also acknowledged.

Appendix. A note on the energy spectra collapse in turbulence generated by active grids

Active-grid experiments can generate relatively high Re_λ turbulence in a typically sized laboratory wind tunnel (Mydlarski & Warhaft 1996) and are thus a potentially good test case to compare the fractal-generated turbulence with. The comparison of the energy decay rate was shown in § 3.4 and here we focus on the collapse of the energy spectra. The data is taken from the experimental investigation by Kang *et al.* (2003) on the decay of active-grid-generated turbulence. In their paper the longitudinal energy spectra for four downstream positions is provided in tabular form and we use this data here to create the plots in figure 20.

The premultiplied longitudinal energy spectra (figure 20) are normalized using both outer ($\overline{u^2}$ and ℓ) and inner (ε and η) variables. Note that ℓ is the pseudo-integral scale defined as $\ell \equiv 0.9u'^3/\varepsilon$ which is proportional to the integral scale if and only if the dissipation coefficient C_ε is constant during decay, in this case $C_\varepsilon = 0.9$.

At a first glance the results seem striking since both outer and inner variables seem to be collapsing the spectra. Thus, one could conjecture that turbulence generated by active grids is self-similar and has only one determining length scale. This would in fact be the case if the Reynolds number Re_λ remained constant during the turbulent kinetic energy decay and consequently $L \propto \lambda \propto \eta$, which is the first ever self-preserving decay proposed (Kármán & Howarth 1938). Instead Re_λ decreases during decay. Hence, this collapse can only be apparent, but not real.

A simple method of estimating the necessary range of Reynolds numbers Re_λ for the collapse to be meaningful is now presented where it is shown that the collapse (or spread) of a normalized spectrum at two streamwise locations is only significant if the logarithm of the respective Reynolds numbers' ratio is large, typically $\log\left(Re_{\lambda_1}/Re_{\lambda_2}\right) > 1/4$. The starting point in this methodology is the assumption that a given scaling is correct (e.g. Kolmogorov or single-length scalings) which then allows the quantification of the spread for a given Re_λ range of any other attempted normalization.

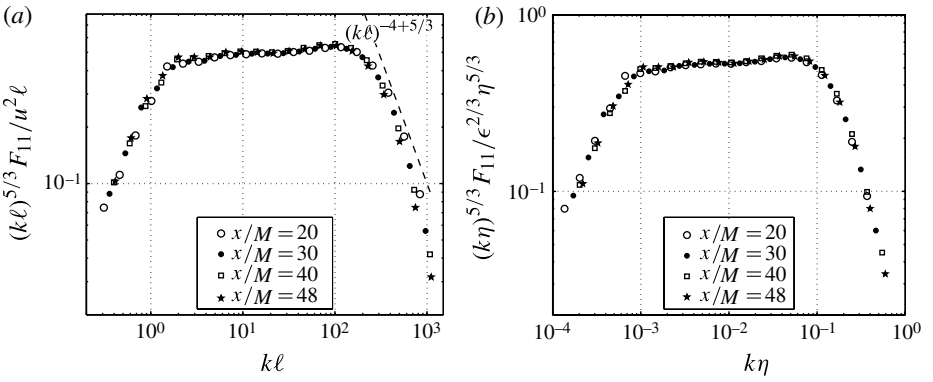

FIGURE 20. Compensated one-dimensional energy spectra at four streamwise locations ($Re_\lambda = 716, 676, 650, 626$) at $U \approx 11$ m s^{-1}, normalized by (*a*) $\overline{u^2}$ and $\ell \equiv 0.9\,u'^3/\varepsilon$ and (*b*) ε and η. Data from Kang *et al.* (2003).

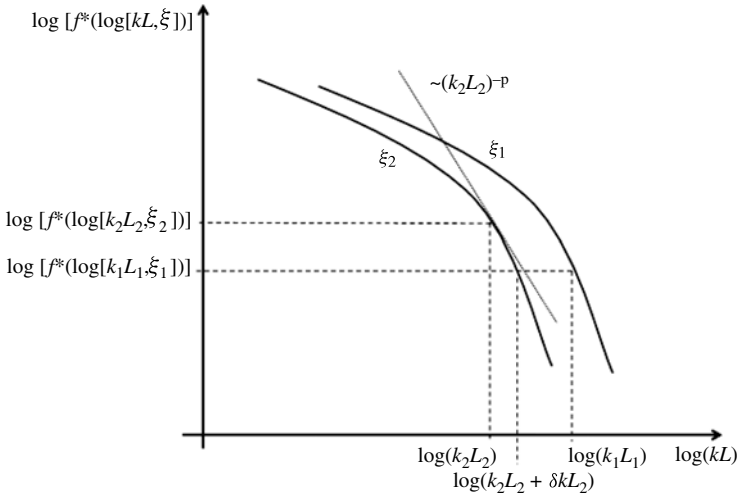

FIGURE 21. Sketch of two spectra at two streamwise positions $x = \xi_1$ and $x = \xi_2$ normalized with outer variables spreading at high frequency.

We outline the method by considering the dissipation range of the longitudinal spectrum and assuming the Kolmogorov scaling is correct, i.e. $F_{11}(k, x) = \varepsilon^{2/3}\eta^{5/3}f(k\eta)$, but this methodology is easily extendable to the energy containing range of the spectrum as well as to the case where the single-length scaling is correct.

Consider two streamwise distances $x = \xi_1$ and $x = \xi_2$ and write $\eta_1 = \eta(\xi_1)$, $\eta_2 = \eta(\xi_2)$, $\lambda_1 = \lambda(\xi_1)$, $\lambda_2 = \lambda(\xi_2)$, $L_1 = L_u(\xi_1)$, $L_2 = L_u(\xi_2)$, $u'_1 = u'(\xi_1)$, $u'_2 = u'(\xi_2)$, $\varepsilon_1 = \varepsilon(\xi_1)$, $\varepsilon_2 = \varepsilon(\xi_2)$ for the Kolmogorov scales, Taylor microscales, integral scales, r.m.s. turbulence velocities and dissipation rates at these two locations. We take $\xi_2 > \xi_1$ so that $Re_{L_1} \equiv u'_1L_1/\nu > Re_{L_2} \equiv u'_2L_2/\nu$.

Choose two wavenumbers k_1 and k_2 in the dissipation range such that $k_1\eta_1 = k_2\eta_2$ and $f(k_1\eta_1) = f(k_2\eta_2)$ by assumption. If one would normalize the same spectra in this range using u'^2 and L_u, the dependence of the normalized spectra on x would

explicitly resurface, i.e. $F_{11}(k,x) = u'^2\, L_u f^*(kL_u, x)$ (see figure 21). Since $\varepsilon = C_\varepsilon u'^3/L_u$ with C_ε independent of x in the Richardson–Kolmogorov phenomenology, it follows that $L_u/\eta = C_\varepsilon^{1/4} Re_L^{3/4}$ and it is possible to show that

$$f^*(k_1L_1, \xi_1) = f^*(k_2L_2, \xi_2)\left(\frac{\eta_1}{L_1}\frac{L_2}{\eta_2}\right)^{5/3} = f^*(k_2L_2, \xi_2)\left(\frac{Re_{L_2}}{Re_{L_1}}\right)^{5/4} \tag{A 1}$$

and

$$k_1L_1 = k_2L_2\left(\frac{\eta_2}{L_2}\frac{L_1}{\eta_1}\right) = k_2L_2\left(\frac{Re_{L_1}}{Re_{L_2}}\right)^{3/4}, \tag{A 2}$$

so that $f^*(k_1L_1, \xi_1) \neq f^*(k_2L_2, \xi_2)$ and $k_1L_1 \neq k_2L_2$.

We define the spectral spread which characterizes the degree of non-collapse by the form $F_{11} = u'^2 L_u f^*(kL_u)$ as

$$\Psi = \log(k_1L_1) - \log(k_2L_2 + \delta kL_2), \tag{A 3}$$

where $f^*(k_1L_1, \xi_1) = f^*(k_2L_2 + \delta kL_2, \xi_2)$, see figure 21. There are two contributions to the spectral spread, one from the rescaling of the abscissas, $k_1L_1 \neq k_2L_2$, and another from the rescaling of the ordinates. From $Re_{L_1} > Re_{L_2}$ and (A 1), (A 2) we know that $k_1L_1 > k_2L_2$ and $f^*(k_1L_1, \xi_1) < f^*(k_2L_2, \xi_2)$ so that the two contributions to the spectral spread can actually, in principle, cancel each other. However, the second contribution depends on the functional form of $f^*(kL_u)$ and therefore it is not possible to quantify its spectral spread contribution without an analytical expression for $f^*(kL_u, \xi)$. Nonetheless, as shown below, we can estimate a bound for this contribution, so that in the end we can estimate a upper and lower bound for the expected spectral spread Ψ characterizing the degree of non-collapse by the alternative scaling.

The contribution to the spread Ψ from the abscissa's rescaling alone (which is the upper bound) is given by (using (A 2))

$$\Psi_{max} = \log(k_1L_1) - \log(k_2L_2) = \frac{3}{4}\log\left(\frac{Re_{L_1}}{Re_{L_2}}\right) = \frac{3}{2}\log\left(\frac{Re_{\lambda_1}}{Re_{\lambda_2}}\right). \tag{A 4}$$

(for the last equality, (1.6) was used to relate the integral scale to the Taylor microscale with $C_\varepsilon = constant$ from Richardson–Kolmogorov phenomenology).

The contribution to the spread Ψ from the ordinate's rescaling is measured as a fraction of the abscissa's rescaling

$$\Phi \equiv \frac{\log(k_2L_2 + \delta kL_2) - \log(k_2L_2)}{\log(k_1L_1) - \log(k_2L_2)}, \tag{A 5}$$

so that $\Phi = 0$ for $\delta kL_2 = 0$ (ordinate rescaling has no effect) and $\Phi = 1$ for $\delta kL_2 = k_1L_1 - k_2L_2$ (ordinate rescaling cancels the abscissas rescaling). It is possible to show using a first-order Taylor expansion in logarithmic coordinates that we can rewrite the function Φ to leading order as

$$\Phi = -\frac{5}{3}\left(\left.\frac{\partial\, \log(f^*(\log(kL_u), \xi))}{\partial\, \log(kL_u)}\right|_{kL_u = k_2L_2}\right)^{-1}. \tag{A 6}$$

Since the spectra in the dissipation range roll-off faster than any power law we can always find a high enough wavenumber $k_t(p)L_u$ for which the tangent of the spectrum

(in logarithmic coordinates) is steeper than $(kL)^{-p}$ given an exponent p (see figure 21). Consequently, for a given choice of p, we get an upper bound for Φ for wavenumbers above $k_t(p)L_u$ which is $\Phi_{max} = 5/(3p)$. Therefore, we can estimate a lower bound for the spectral spread as $\Psi_{min} = \Psi_{max} - \Phi_{max}$ and thus

$$\frac{3}{2}\log\left(\frac{Re_{\lambda_1}}{Re_{\lambda_2}}\right) - \frac{5}{3p} < \Psi < \frac{3}{2}\log\left(\frac{Re_{\lambda_1}}{Re_{\lambda_2}}\right). \tag{A 7}$$

In figure 20(*a*) we plot the $(kL_u)^{-p}$ function with $p = 4$ and it can be seen that for wavenumbers higher than $k_tL_u \approx 400$, the tangent of the spectra (in logarithmic coordinates) are steeper. Hence, according to (A 7), for $k_tL_u > 400$ (taking into account the Re_λ range of the data presented in figure 20*a*) the spectral spread will be around $5\,\% < \Psi < 9\,\%$ of a decade, which can easily be confounded with scatter. Therefore, the apparent collapse observed in the spectra from the active-grid experiments of Kang *et al.* (2003) (see figure 20*a*) may be misleading as it is simply the result of a small range of Re_λ variation during decay (from 716 to 637). Note that the same misleading collapse occurs in the low wavenumber range of the spectra plotted in figure 20(*b*) where the Kolmogorov inner variables were used for the normalization.

We can repeat the exact same analysis for the case where the Richardson–Kolmogorov cascade is suppressed and assume the validity of $F_{11}(k, x) = u'^2L_uf^*(kL_u)$ and $L_u/\lambda \approx constant$. We can then carry out the same calculation as above to obtain the spectral spread $\Psi = \log(k_1\eta_1) - \log(k_2\eta_2 + \delta k\eta_2)$ for $k_1L_1 = k_2L_2$ when attempting to collapse the data with Kolmogorov variables. We would then obtain the same expression to quantify the spread contribution caused by the rescaling of the ordinates relative to the total spread, (A 5) with a suitably redefined Φ where the outer scales L_u have been replaced by inner scales η. Note that spread of the high-frequency spectra normalized by outer variables assuming that $F_{11}(k, x) = \varepsilon^{2/3}\eta^{5/3}f(k\eta)$ holds is the same as the spread of the high-frequency spectra normalized by Kolmogorov inner variables assuming that $F_{11}(k, x) = u'^2L_uf^*(kL_u)$ holds. Hence, using $L_u \sim \lambda$, the spectral spread resulting from an attempt to collapse with Kolmogorov inner variables spectra which obey complete self-similarity is

$$\Psi = \log(k_1\eta_1) - \log(k_2\eta_2) = \frac{1}{2}\log\left(\frac{Re_{\lambda_1}}{Re_{\lambda_2}}\right). \tag{A 8}$$

It is interesting to observe that the rate of spread in this case is three times slower than the rate of spread when the Richardson–Kolmogorov cascade dominates and one tries to collapse with outer variables. Hence, the spectral spread observed in figure 14(*a*) is in agreement with the view that RG turbulence at the Reynolds numbers of this figure obeys Richardson–Kolmogorov interscale dynamics. However, the high-frequency behaviours in figures 14(*b*), 15(*b*) and 15(*c*) fall within the uncertainty defined by (A 8) and we are therefore unable to conclude whether our fractal-grid-generated turbulence obeys complete or incomplete self-similarity even though it is clear that $L_u \propto \lambda$ is a good approximation. By complete self-similarity we refer to the property that $F_{11}(k, x) = u'^2L_uf^*(kL_u)$ is exact at all frequencies and by incomplete self-similarity we refer to the property that deviations to $F_{11}(k, x) = u'^2L_uf^*(kL_u)$ can appear at the very highest frequencies. We stress that this does not imply Kolmogorov scaling even if these high frequencies may be collapsed by Kolmogorov inner variables for the simple reason that $L_u \propto \lambda$ and therefore ε is not proportional to u'^3/L_u.

REFERENCES

ANTONIA, R. A. 2003 On estimating mean and instantaneous turbulent energy dissipation rates with hot wires. *Exp. Therm. Fluid Sci.* **27**, 151–157.

ANTONIA, R. A., SMALLEY, R. J., ZHOU, T., ANSELMET, F. & DANAILA, L. 2003 Similarity of energy structure functions in decaying homogeneous isotropic turbulence. *J. Fluid Mech.* **487**, 245–269.

BATCHELOR, G. K. 1953 *The Theory of Homogeneous Turbulence*. Cambridge University Press.

BATCHELOR, G. K. & TOWNSEND, A. A. 1948 Decay of isotropic turbulence in the initial period. *Proc. R. Soc.* A **193** (1035), 539–558.

BURATTINI, P., LAVOIE, P. & ANTONIA, R. A. 2005 On the normalized turbulent energy dissipation rate. *Phys. Fluids* **17**, 098103.

COMTE-BELLOT, G. & CORRSIN, S. 1966 The use of a contraction to improve the isotropy of grid-generated turbulence. *J. Fluid Mech.* **25** (04), 657–682.

CORRSIN, S. 1963 *Handbook der Physik*. Springer.

DIMOTAKIS, P. E. 2000 The mixing transition in turbulent flows. *J. Fluid Mech.* **409**, 69–98.

ERTUNÇ, Ö., ÖZYILMAZ, N., LIENHART, H., DURST, F. & BERONOV, K. 2010 Homogeneity of turbulence generated by static-grid structures. *J. Fluid Mech.* **654** (1), 473–500.

FREYMUTH, P. 1977 Frequency response and electronic testing for constant-temperature hot-wire anemometers. *J. Phys. E: Sci. Instrum.* **10**, 705.

FRISCH, U. 1995 *Turbulence: The Legacy of AN Kolmogorov*. Cambridge University Press.

GAMARD, S. & GEORGE, W. K. 2000 Reynolds number dependence of energy spectra in the overlap region of isotropic turbulence. *Flow Turbul. Combust.* **63** (1), 443–477.

GEIPEL, P., HENRY GOH, K. H. & LINDSTEDT, R. P. 2010 Fractal-generated turbulence in opposed jet flows. *Flow Turbul. Combust.* **85** (3–4), 397–419.

GEORGE, W. K. 1992 The decay of homogeneous isotropic turbulence. *Phys. Fluids* A **4** (7), 1492–1509.

GEORGE, W. K. & WANG, H. 2009 The exponential decay of homogeneous turbulence. *Phys. Fluids* **21**, 025108.

GOTO, S. & VASSILICOS, J. C. 2009 The dissipation rate coefficient of turbulence is not universal and depends on the internal stagnation point structure. *Phys. Fluids* **21**, 035104.

HELLAND, K. N. & VAN ATTA, C. W. 1977 Spectral energy transfer in high Reynolds number turbulence. *J. Fluid Mech.* **79** (02), 337–359.

HURST, D. J. & VASSILICOS, J. C. 2007 Scalings and decay of fractal-generated turbulence. *Phys. Fluids* **19**, 035103.

ISHIDA, T., DAVIDSON, P. A. & KANEDA, Y. 2006 On the decay of isotropic turbulence. *J. Fluid Mech.* **564**, 455–475.

JAYESH, & WARHAFT, Z. 1992 Probability distribution, conditional dissipation, and transport of passive temperature fluctuations in grid-generated turbulence. *Phys. Fluids* A **4**, 2292.

KAHALERRAS, H., MALECOT, Y., GAGNE, Y. & CASTAING, B. 1998 Intermittency and Reynolds number. *Phys. Fluids* **10**, 910.

KANG, H., CHESTER, S. & MENEVEAU, C. 2003 Decaying turbulence in an active-grid-generated flow and comparisons with large-eddy simulation. *J. Fluid Mech.* **480**, 129–160.

KÁRMÁN, T. & HOWARTH, L. 1938 On the statistical theory of isotropic turbulence. *Proc. R. Soc.* A **164** (917), 192–215.

KINZEL, M., WOLF, M., HOLZNER, M., LÜTHI, B., TROPEA, C. & KINZELBACH, W. 2011 Simultaneous two-scale 3D-PTV measurements in turbulence under the influence of system rotation. *Exp. Fluids* **51** (1), 75–82.

KISTLER, A. L. & VREBALOVICH, T. 1966 Grid turbulence at large Reynolds numbers. *J. Fluid Mech.* **26**, 37–47.

KOLMOGOROV, A. N. 1941 The local structure of turbulence in incompressible viscous fluid for very large Reynolds. *C. R. Acad. Sci. U. R. S. S.* **30**, 301.

KROGSTAD, P. Å. & DAVIDSON, P. A. 2011 Freely decaying, homogenous turbulence generated by multi-scale grids. *J. Fluid Mech.* **680**, 417–434.

LAIZET, S. & VASSILICOS, J. C. 2011 Dns of fractal-generated turbulence. *Flow Turbul. Combust* doi:10.1007/s10494-011-9351-2.

LAVOIE, P., DJENIDI, L. & ANTONIA, R. A. 2007 Effects of initial conditions in decaying turbulence generated by passive grids. *J. Fluid Mech.* **585**, 395–420.

LESIEUR, M. 1997 *Turbulence in Fluids*. Kluwer Academic.

LUMLEY, W. K. 1992 Some comments on turbulence. *Phys. Fluids* A **4** (2), 203–211.

MAKITA, H. 1991 Realization of a large-scale turbulence field in a small wind tunnel. *Fluid Dyn. Res.* **8**,.

MATHIEU, J. & SCOTT, J. 2000 *An Introduction to Turbulent Flows*. Cambridge University Press.

MAZELLIER, N. & VASSILICOS, J. C. 2008 The turbulence dissipation constant is not universal because of its universal dependence on large-scale flow topology. *Phys. Fluids* **20**, 015101.

MAZELLIER, N. & VASSILICOS, J. C. 2010 Turbulence without Richardson–Kolmogorov cascade. *Phys. Fluids* **22**, 075101.

MOHAMED, M. S. & LARUE, J. C. 1990 The decay power law in grid-generated turbulence. *J. Fluid Mech.* **219**, 195–214.

MYDLARSKI, L. & WARHAFT, Z. 1996 On the onset of high-Reynolds-number grid-generated wind tunnel turbulence. *J. Fluid Mech.* **320**, 331–368.

NAGATA, K., SUZUKI, H., SAKAI, Y., HAYASE, T. & KUBO, T. 2008*a* Direct numerical simulation of turbulent mixing in grid-generated turbulence. *Phys. Scr.* **2008**, 014054.

NAGATA, K., SUZUKI, H., SAKAI, Y., HAYASE, T. & KUBO, T. 2008*b* DNS of passive scalar field with mean gradient in fractal-generated turbulence. *Int. Rev. Phys.* **2**, 400.

PEARSON, B. R., KROGSTAD, P.-Å. & VAN DE WATER, W. 2002 Measurements of the turbulent energy dissipation rate. *Phys. Fluids* **14**, 1288.

POPE, S. B. 2000 *Turbulent Flows*. Cambridge University Press.

QUEIROS-CONDE, D. & VASSILICOS, J. C. 2001 *Intermittency in Turbulent Flows and Other Dynamical Systems*. Cambridge University Press.

ROTTA, J. C. 1972 *Turbulente Strömungen: eine Einführung in die Theorie und ihre Anwendung*. B.G. Teubner.

SAGAUT, P. & CAMBON, C. 2008 *Homogeneous Turbulence Dynamics*. Cambridge University Press.

SCHEDVIN, J., STEGEN, G. R. & GIBSON, C. H. 1974 Universal similarity at high grid Reynolds numbers. *J. Fluid Mech.* **65** (03), 561–579.

SEOUD, R. E. & VASSILICOS, J. C. 2007 Dissipation and decay of fractal-generated turbulence. *Phys. Fluids* **19**, 105108.

SREENIVASAN, K. R. 1984 On the scaling of the turbulence energy dissipation rate. *Phys. Fluids* **27**, 1048.

SREENIVASAN, K. R. 1998 An update on the energy dissipation rate in isotropic turbulence. *Phys. Fluids* **10**, 528.

STRESING, R., PEINKE, J., SEOUD, R. E. & VASSILICOS, J. C. 2010 Defining a new class of turbulent flows. *Phy. Rev. Lett.* **104** (19), 194501.

SUZUKI, H., NAGATA, K., SAKAI, Y. & UKAI, R. 2010 High-Schmidt-number scalar transfer in regular and fractal grid turbulence. *Phys. Scr.* **2010**, 014069.

TAYLOR, G. I. 1935 Statistical theory of turbulence. *Proc. R. Soc.* A **151** (873), 421–444.

TENNEKES, H. & LUMLEY, J. L. 1972 *A First Course in Turbulence*. MIT.

TOWNSEND, A. A. 1956 *The Structure of Turbulent Shear Flow*. Cambridge University Press.

UBEROI, M. S. 1963 Energy transfer in isotropic turbulence. *Phys. Fluids* **6** (8), 1048–1056.

VASSILICOS, J. C. 2011 An infinity of possible invariants for decaying homogeneous turbulence. *Phys. Lett.* A **6**, 1010–1013.

WANG, H. & GEORGE, W. K. 2002 The integral scale in homogeneous isotropic turbulence. *J. Fluid Mech.* **459**, 429–443.